Department of Radio Science and Engineering

Radar polarimetry and interferometry for remote sensing of boreal forest

Jaan Praks

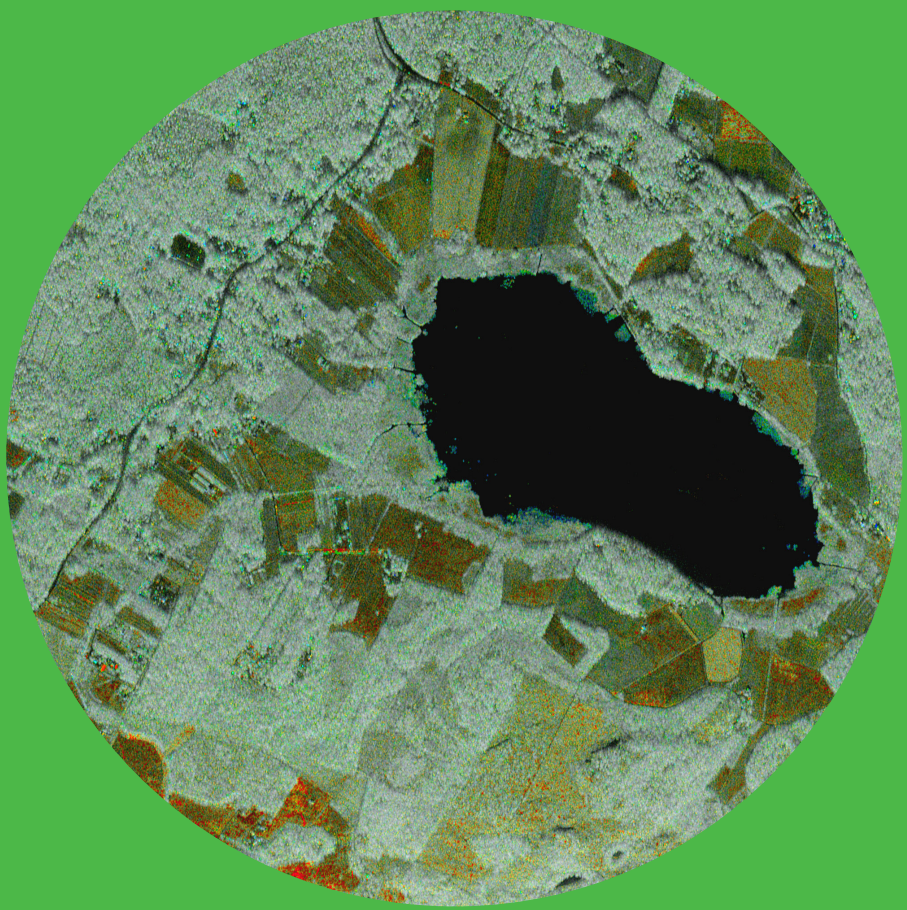

Aalto University

DOCTORAL DISSERTATIONS

Aalto University publication series
DOCTORAL DISSERTATIONS 153/2012

Radar polarimetry and interferometry for remote sensing of boreal forest

Jaan Praks

A doctoral dissertation completed for the degree of Doctor of Science (Technology) to be defended, with the permission of the Aalto University School of Electrical Engineering, at a public examination held at the lecture hall S4 of the school on 23 November 2012 at 12.

Aalto University
School of Electrical Engineering
Department of Radio Science and Engineering
Space Technology

Supervising professor
Prof. Martti Hallikainen

Preliminary examiners
Prof. Erkki Tomppo
Dr Iain H. Woodhouse

Opponent
Prof. Juan Manuel López-Sánchez

Aalto University publication series
DOCTORAL DISSERTATIONS 153/2012

ISBN 978-952-60-4872-7 (printed)
ISBN 978-952-60-4873-4 (pdf)
ISSN-L 1799-4934
ISSN 1799-4934 (printed)
ISSN 1799-4942 (pdf)
http://urn.fi/URN:ISBN:978-952-60-4873-4

Unigrafia Oy
Helsinki 2012

Finland

441 697
Printed matter

Author
Jaan Praks

Name of the doctoral dissertation
Radar polarimetry and interferometry for remote sensing of boreal forest

Publisher School of Electrical Engineering

Unit Department of Radio Science and Engineering

Series Aalto University publication series DOCTORAL DISSERTATIONS 153/2012

Field of research Space technology and remote sensing

Manuscript submitted 7 June 2012 **Date of the defence** 23 November 2012

Permission to publish granted (date) 11 September 2012 **Language** English

☐ **Monograph** ☒ **Article dissertation (summary + original articles)**

Abstract

Forest biomass is a key parameter of the global biosphere which is linked to many fields of research. Modeling addressing climate, ecology, and economics as well as many other prediction frameworks require an accurate assessment of global forest biomass. Methods for producing forest information are rapidly developing and traditional forest inventory by visual estimation has been gradually replaced by the use of airborne and spaceborne instruments. Nevertheless, the estimation of biomass on a global basis including boreal, temperate, and tropical forests, is still a major challenge. Among other spaceborne sensors, synthetic aperture radar (SAR) is one of the most suitable tools for large scale mapping and it has also been often used for forest mapping. However, commonly used backscattering intensity based methods do not provide a satisfactory accuracy for biomass estimation; hence, the scientific radar community has been developing more accurate means based on advanced SAR imaging and analyzing techniques, such as SAR polarimetry and interferometry.

The work within this thesis contributes to this effort specifically in the field of remote sensing with the emphasis on SAR polarimetry and interferometry for boreal forest applications. The study concentrates on three main topics: polarimetric SAR image analysis, retrieval of forest height by means of SAR interferometry, and modeling of radar backscattering from trees. The main contributions of this work include a new effective approach in polarimetric target decomposition, novel polarimetric visualization schemes, an improved interferometric tree height estimation method suitable for boreal forest, interferometric tree height estimation capability demonstration for X-band, a novel method for relating SAR measurements to single tree scattering modeling, and taking the scattering modeling from a pine tree to the single needle level with accurate field models.

Furthermore, the forest height estimation scheme proposed in this work potentially enables tree height estimation with existing spaceborne interferometric X-band SAR systems. The proposed method uses an interferometric coherence model and a ground elevation model to produce accurate tree height maps from single polarization interferometric SAR data. The method is demonstrated with airborne SAR measurements and will be tested in the near future with satellite data. Since tree height is related to forest biomass through tree allometry, tree height measurements from space would enable more accurate global forest biomass maps.

Keywords Radar, Synthetic Aperture Radar, SAR, SAR polarimetry, SAR interferometry, SAR polarimetric interferometry, InSAR, PolSAR, Pol-InSAR, boreal forest, scattering model, tree height, forest height, forest biomass

ISBN (printed) 978-952-60-4872-7 **ISBN (pdf)** 978-952-60-4873-4

ISSN-L 1799-4934 **ISSN (printed)** 1799-4934 **ISSN (pdf)** 1799-4942

Location of publisher Espoo **Location of printing** Helsinki **Year** 2012

Pages 167 **urn** http://urn.fi/URN:ISBN:978-952-60-4873-4

Preface

Working on this thesis has been a colorful journey that has included many fascinating detours which have allowed me to meet many interesting and delightful people. First of all, I would like to thank my supervisor Martti Hallikainen who has given me this opportunity and guided me over many obstacles during the voyage.

I would also like to give my thanks to Andres Kuusk and Tiit Nilson who long ago in Tartu introduced me to the wonderful world of Earth Observation, and to Jarkko Koskinen as well who assigned me a task to analyze polarimetric SAR images. My gratitude belongs to my co-authors and colleagues, namely: to Elise Colin for introducing me to optical polarimetry; to Kostas Papathanassiou, Florian Kugler and Irena Hajnsek for introducing me to polarimetric interferometry; to Oleg Antropov for testing my wild ideas; and to Tommi Dufva, Jukka Sarvas, Seppo Järvenpää and Jouni Pulliainen for helping me to model radar responses from a beautiful pine tree. Special thanks goes to Juha Hyyppä who provided me with an accurate terrain model, to Jari Perttunen who gave me LIGNUM trees, to Toomas Altosaar who helped with proof reading and to everybody who participated in the FINSAR campaign.

For financial support I am grateful to the Wihuri foundation, for TES who helped me to attend conferences, to the GETA graduate school, and to the Academy of Finland and TEKES who financed these interesting projects. Last but not least, my sincere gratitude to my wife Juuli.

Espoo, October 31, 2012,

Jaan Praks

Contents

List of Publications

This thesis consists of an overview and of the following publications which are referred to in the text by their Roman numerals.

I Jaan Praks, Elise Colin-Koeniguer, Martti Hallikainen. Alternatives to target entropy and alpha angle in SAR polarimetry. *IEEE Transactions on Geoscience and Remote Sensing*, 47(7):2262–2274, July 2009.

II Jaan Praks, Florian Kugler, Konstantinos Papathanassiou, Irena Hajnsek, Martti Hallikainen. Height estimation of boreal forest: interferometric model-based inversion at L- and X-band versus HUTSCAT profiling scatterometer. *IEEE Geoscience and Remote Sensing Letters*, 4(3):466–470, July 2007.

III Jaan Praks, Oleg Antropov, Martti Hallikainen. LIDAR-aided polarimetric SAR interferometry studies in boreal forest: phase center and extinction coefficient at X- and L-band. *IEEE Transactions on Geoscience and Remote Sensing*, 50(10):3831–3843, October 2012.

IV Jaan Praks, Jukka Sarvas, Martti Hallikainen, Jouni Pulliainen. Using multilook averaging for coherently modeled scattering from a pine tree at L-band. *IEEE Geoscience and Remote Sensing Letters*, 6(1):162–166, January 2009.

V Tommi Dufva, Jaan Praks, Seppo Järvenpää, Jukka Sarvas. Scattering model for a pine tree employing VIE with a broadband MLFMA and comparison to ICA. *IEEE Transactions on Geoscience and Remote Sens-*

ing, 48(3):1119–1127, March 2010.

Author's Contribution

Publication I: "Alternatives to target entropy and alpha angle in SAR polarimetry"

This work was done jointly by the author and Elise Colin-Koeniguer from ONERA, France. The idea of using simpler alternatives for polarimetric target entropy and alpha values was first proposed by the author in [45]. The idea was developed further in [46, 47, 48] by introducing matrix similarity invariants and visualization schemes in [49]. Elise Colin-Koeniguer contributed with the in depth analysis of relations between polarimetric covariance matrices and also the analysis of linkages to optical polarimetry [10]. The original idea of the paper was proposed by the author.

Publication II: "Height estimation of boreal forest: interferometric model-based inversion at L- and X-band versus HUTSCAT profiling scatterometer"

This work was done by the author in cooperation with Florian Kugler and Konstantinos Papathanassiou from Microwaves and Radar Institute, DLR, Germany. The work was part of an effort to analyze FINSAR campaign measurements with the aim to develop interferometric and polarimetric methods for forest remote sensing. The author participated in the arrangement of airborne and field campaigns, analyzed ground and HUTSCAT measurements, extracted tree height estimates from HUTSCAT measurement and made the comparison between HUTSCAT and E-SAR forest height estimates. Tree height estimation by RVoG model inversion based on E-SAR measurements was in this work performed mainly by the co-authors. The work with the dataset was reported also

in [52, 50, 51, 54, 53] and in Publication III.

Publication III: "LIDAR-aided polarimetric SAR interferometry studies in boreal forest: phase center and extinction coefficient at X- and L-band"

This publication was made mainly by the author, however, co-authors helped with the cross testing of the modeling approach and helped with editorial work as well. Oleg Antropov also contributed with the idea of lookup tables for forest extinction coefficients for different forest classes. This work continued the previous work with the FINSAR dataset as reported in Publication II. Some of preprocessing of E-SAR data was made in DLR and LIDAR measurements were provided in geocoded form by the Finnish Geodetic Institute. The original idea of the paper was proposed by the author.

Publication IV: "Using multilook averaging for coherently modeled scattering from a pine tree at L-band"

This work was formed as a part of the larger MODAFOR project, where Rolf Nevanlinna Institute and Helsinki University of Technology developed mathematical tools for forest modeling. The ICA model used in the paper was mainly developed by the co-authors with a contribution from the author. The author performed calculations with the model, constructed the tree model from LIGNUM data, and carried out statistical analysis of the model output. The original idea of statistics calculation with tree rotation was proposed by the author.

Publication V: "Scattering model for a pine tree employing VIE with a broadband MLFMA and comparison to ICA"

This work was a collaborative effort. The main work with VIE model development and calculations were done by the first author, Tommi Dufva. The author of this thesis made all the ICA model calculations and built the cylinder model of the tree by using LIGNUM tree growth model data. The author also contributed to the development of the comparison method and to the interpretation of the results.

List of Figures

List of Abbreviations

AIRSAR	AIRborne Synthetic Aperture Radar (JPL, USA)
BSA	Back Scattering Alignment
C-band	Frequencies 4 GHz – 8 GHz
CHM	Canopy Height Model
CIE	International Commission on Illumination
DEM	Digital Elevation Model
DLR	Deutsches Zentrum für Luft- und Raumfahrt – German Aerospace Center
E-SAR	Airborne radar system (DLR, Germany)
EO	Earth Observation
FINSAR	Airborne SAR measurement campaign in Finland
FSA	Forward Scattering Alignment
HSI	Hue Saturation Intensity
HUTSCAT	Helsinki University of Technology SCATterometer
ICA	Infinite Cylinder Approximation
InSAR	Interferometric SAR
JPL	Jet Propulsion Laboratory (USA)
L-band	Frequencies 1 GHz – 2 GHz
LIDAR	LIght Detection and Ranging
LIGNUM	A fractal like functional-structural tree model

MLFMA	Multi-Level Fast Multipole Algorithm
MODAFOR	new MOdeling and Data Analysis methods for satellite based FORest inventory (project)
ONERA	Office National d'Études et de Recherches Aérospatiale – French Aerospace Research Center
Pol-InSAR	Polarimetric interferometric SAR
PolSAR	Polarimetric SAR
RADAR	RAdio Detection And Ranging
RGB	Red Green Blue
RVoG	Random Volume over Ground
SAR	Synthetic Aperture Radar
TanDEM-X	TerraSAR-X Add-oN for Digital Elevation Measurement
TerraSAR-X	Earth Observation SAR satellite (Germany)
TKK	Helsinki University of Technology (presently forms part of Aalto University)
UHF-band	Frequencies 300 MHz – 1000 MHz
VIE	Volume Integral Equation
X-band	Frequencies 8 GHz – 12 GHz

List of Symbols

α_n, β_n, δ_n	Eigenvector orientation angles
$\bar{\alpha}$	Average scattering mechanism
γ	Interferometric complex coherence
γ_m	Modeled interferometric coherence
γ_v	Volume induced complex coherence
ϵ	Permittivity
ϵ_{soil}	Permittivity of soil
ϵ_{tree}	Permittivity of tree
θ_0	Incidence angle
κ	Wavenumber
κ_z	Vertical wavenumber
λ	Radar wavelength
$\lambda_1, \lambda_2, \lambda_3$	Coherency matrix eigenvalues
σ	Radar cross section
σ_m	Local extinction coefficient of volume
σ_v	Extinction coefficient of volume
ϕ_0	Ground phase
ϕ_f	Constant for DEM fitting
ϕ_γ	Interferometric phase

A_r	Receiving antenna aperture
A_{rs}	Target aperture
a, b, c, d	Pauli decomposition weights
$\mathbf{C}$	Covariance matrix
$\vec{E}_i$	Incident electric field
$\vec{E}_s$	Scattered electric field
F	Scattering matrix in FSA
$_{Fr}$	Frobenius norm, when in subscript
f_a	Target absorption coefficient
G_t	Transmitting antenna gain
G_{ts}	Target gain
$\hat{H}$	Scattering diversity
H	Target entropy
h_f	Constant for DEM fitting
$_H$	Horizontal polarization, when in subscript
H'	Target entropy approximation
h_v	Forest volume layer height
$\mathbf{I}$	Identity matrix
$\hat{k}$	Direction vector
$\vec{k}$	Scattering vector
$\vec{k}_1, \vec{k}_2, \vec{k}_3$	Coherency matrix eigenvectors
M	Ground-to-volume scattering ratio
m_G	Ground scattering amplitude
m_v	Volume scattering amplitude
m	Indexing variable
$\mathbf{N}$	Power normalized coherency matrix

N_{11}	Surface scattering fraction
N_{mn}	Element of power normalized coherency matrix
n	Indexing variable
P	Probability
p	Polarization, when in subscript
P_r	Radar received power
P_t	Radar transmitted power
p	Scattering mechanism probability
q	Polarization, when in subscript
R_r	Radar receiving antenna distance from target
R_t	Radar transmitting antenna distance from target
$\mathbf{S}$	Scattering matrix in BSA
S_{qp}	Scattering matrix element
$span$	Total backscattered power, covariance matrix trace
$\mathbf{T}$	Coherency matrix
U	Unitary rotation matrix
v	Vertical polarization, when in subscript
W	Modeled scatterer
$\vec{w}$	Radar polarization
z_n	Eigenvector phase

1. Introduction

Remote sensing is a field of science and technology which deals with measurements of large scale objects, mostly from airborne and spaceborne platforms. It is often the only means to gain information about large, planetary scale processes. Typical applications of remote sensing are mapping of large land areas, water bodies, atmosphere, and large scale human activities.

Remote sensing as a scientific discipline is a rather young field. The first attempts to acquire images over larger areas were possible when photography was just evolving around 150 years ago. Joined together with the state of aeronautics at the time, the first optical cameras were mounted onto balloons. Rapid development of remote sensing technology has continued hand in hand with aeronautical and space technology developments and has become an integral part of our everyday life. Cloud maps measured by satellite sensors appear in TV weather forecasts, people browse satellite maps on their navigation systems, and almost everyone knows how our home planet looks like when observed from space. Satellite based instruments provide a global view to the entire planet and the broad perspective helps us to understand and model large scale processes which influence our future.

Most remote sensing instruments use either the visible or microwave spectrum of electromagnetic waves for imaging, due to good penetration through Earth's atmosphere. Microwave radar, with its all-seasonal, all-day, and nearly all-weather high resolution imaging capability, offers unique opportunities for Earth Observation (EO). This particularly concerns Synthetic Aperture Radar (SAR) technology, which is presently an area of active research. With recently launched SAR instruments offering new imaging modes (multi-polarization, multi-frequency, multi-antenna, etc.), focus has shifted to exploitation of novel imaging techniques: SAR po-

larimetry, interferometry, polarimetric SAR interferometry, tomography, and advanced modeling of radar scattering. These new techniques have brought along new possibilities for remote sensing of global vegetation. Compared to optical sensors, SAR reveals different features of vegetation due to its much longer wavelength. Microwaves interact directly with vegetation structure and the coherent nature of the SAR measurement allows one to study structural parameters with the help of polarization measurements and interferometric patterns. However, microwave signal interaction with complex vegetation structure still needs significant research in order to provide operational applications.

One of the areas where a significant benefit from new SAR technologies could be gained is remote sensing of forest, including boreal forest, which is a main topic in this work. Boreal forest is the largest terrestrial biome. It is located in the zone where global climate change can introduce large changes. Boreal forest holds a significant amount of the world's total biomass and is one of the important links in the global carbon cycle. The international scientific community has made significant efforts to harness SAR technology for more accurate forest remote sensing operational applications. Research in this field is constantly growing.

The work presented in this thesis is a part of this international scientific effort, aiming towards more accurate forest maps on a global scale. The work makes a contribution in three main areas: utilizing the information content in the polarimetric SAR image, improving interferometric techniques for forest measurements, and understanding the scattering from forest and trees at a theoretical level. The main contributions of this work to the field of SAR polarimetry and interferometry include a new effective approach in incoherent target decomposition (Publication I), novel polarimetric visualization schemes (Publication I), an improved tree height estimation method suitable for boreal forest (Publication III), demonstration of X-band SAR tree height measurement capability (Publication II), a method to relate SAR measurements to single tree modeling (Publication IV), and calculation of scattering from a pine tree with high accuracy by taking into account single needles (Publication V).

The work is organized as follows. In Chapter 2, an introduction to SAR remote sensing is given. Chapter 3 concentrates on the author's contribution to SAR polarimetry, polarimetric decompositions, and image visualization. An overview of polarimetric decompositions is provided and connections between various polarimetric parameters are explained. New

simpler parameters for polarimetric analysis are proposed and their impact on classification and interpretation is given. In Chapter 4 polarimetric SAR interferometry techniques are developed for boreal forest remote sensing. The work is based on data acquired by the German E-SAR system during an airborne campaign in Finland. An overview of the study material and the main theoretical framework for analysis, including the Random Volume over Ground model, is given. Forest height is effectively retrieved by a novel inversion technique, developed by the author. This method potentially allows tree height measurement by spaceborne X-band SAR. Chapter 5 concentrates on the modeling of radar scattering from trees, clarifying the behavior of the scattering mechanism in both C- and L-bands. It involves, for the first time, calculation of an accurate scattering model accounting for all individual needles in a tree's shoot. Finally, the achieved results of the work are summarized and future work is outlined in Chapter 6. The five publications describing the main body of this work are included at the end of the thesis. In the publications a slightly different mathematical notation is sometimes used when compared to the thesis summary.

2. Synthetic Aperture Radar in Earth Observation applications

In this chapter a very brief overview of SAR remote sensing is given to a reader who is not familiar with the field of radar remote sensing. The chapter explains the most central concepts on which the thesis is built. The first section provides the operational principle of radar while the second section explains the basic idea of Synthetic Aperture Radar (SAR). The third section gives a general background concerning SAR applications and measurement techniques.

2.1 Radar

Radar transmits and receives radio waves to detect object location, movement or reflectivity related properties. The name radar comes from an acronym, which stands for RAdio Detection And Ranging, but the word is used nowadays as a noun. Radars are used widely to detect and guide vehicles (navigation and ranging radars), to measure atmospheric phenomena (weather and precipitation radars) and to image the surrounding environment (remote sensing radars). Radar transmits pulses of electromagnetic radiation and records the reflected echoes, which are just a tiny fraction of the transmitted signal's power. In the most general form, a radar measurement can be described with an equation which gives the received power P_r as a function of transmitted power P_t and measurement setup parameters as

$$P_r = \frac{P_t G_t A_r \sigma}{(4\pi)^2 R_t^2 R_r^2}. \tag{2.1}$$

In Equation (2.1) R_t and R_r stand for transmitting and receiving antenna distances from the object, G_t stands for transmitting antenna gain, A_r is receiving antenna effective aperture and σ describes the properties of the measured object. In radar community σ is called the *radar cross section* of the target and it depends on the object's ability to receive and reflect

the radiation (described by its gain G_{ts} and aperture A_{rs}) in the radar's antenna direction and losses of energy in the object (described by the absorption coefficient f_a). The radar cross section of an object depends additionally on the radar wavelength λ and polarization w of the incident wave,

$$\sigma(\lambda, \vec{w}) = [A_{rs}(1 - f_a)G_{ts}]\,. \tag{2.2}$$

The radar cross section is a fundamental entity in radar remote sensing.

2.2 Synthetic Aperture Radar (SAR)

Synthetic Aperture Radar (SAR) is an advanced imaging radar system which uses coherent microwave signals to illuminate a target or an area and forms an image of the scene. SAR provides much higher spatial resolution than its physical antenna size would permit by utilizing antenna movement and a technique called *aperture synthesis* where a virtual antenna along the real antenna trajectory is formed by combining several measurements along the movement path. The antenna movement direction is called *azimuth direction* and the resolution in this direction is achieved with synthetic aperture by separating reflections from different areas according to the Doppler frequency shift. The direction perpendicular to the movement direction is called *range direction* and in this direction good resolution is achieved by accounting for the reflected pulse delay in time. In order to avoid ambiguity between reflections from the same distance, SAR only looks to one side from the platform. Figure 2.1 explains the basic concepts of SAR imaging geometry.

The SAR image is a map, which describes the spatial distribution of the target's reflective properties. An example of a SAR image is shown in Figure 2.2.

SAR instruments for remote sensing applications typically use wavelengths ranging from several decimeters to a few centimeters. The wavelength of the radar is significantly longer than in optical sensors and therefore the radar sees the world rather differently. The radar pulse interacts only with structural entities larger than the radar's wavelength. Opposite to optical instruments, the radar also cannot see "colors" i.e. respective frequency dependent features as it uses only a single coherent frequency for sensing. The Radar operational frequency range is divided into bands, denoted for historical reasons by letters. Common re-

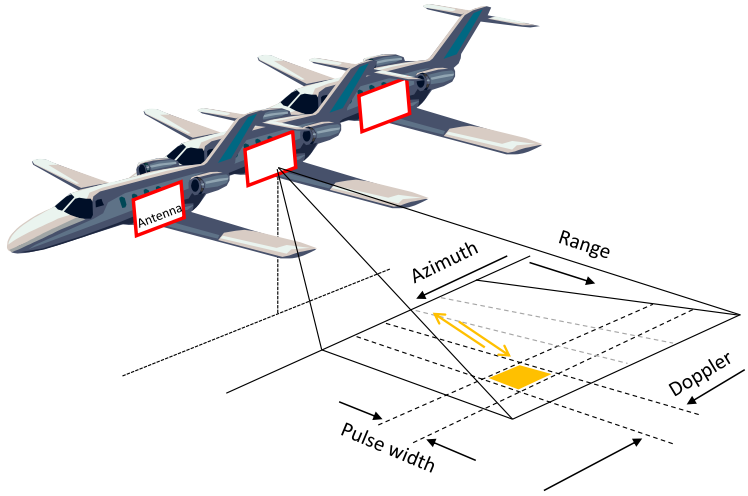

Figure 2.1. Synthetic Aperture Radar imaging geometry. The virtual antenna is formed by combining several measurements along the movement path.

mote sensing radars can operate e.g. in the UHF-band (wavelength 69 cm at frequency 435 MHz), L-band (wavelength 25 cm at 1.2 GHz), C-band (wavelength 5.7 cm at frequency 5.3 GHz) and in the X-band (wavelength 3.1 cm at frequency 9.6 GHz). For these wavelength ranges the atmosphere is basically transparent; the effect of clouds increases with frequency, but does not prevent measurement.

2.3 Interferometric and polarimetric SAR techniques in Earth Observation

SAR systems are used increasingly in Earth Observation applications, due to their high resolution, nearly all weather imaging capability and independence of solar illumination. Numerous Earth Observation satellites carry SAR instruments and the most recent SAR systems fly in constellations in order to utilize more complex multi antenna imaging techniques. SAR applications range from simple roughness detection to advanced 3D tomographic techniques. SAR images are used for ship detection, forestry, ice and glacier research, polar area monitoring, crop classification, urban mapping, terrain elevation model measurements and in many other areas [30].

Many modern SAR systems also measure the dependence of the target's backscattering on the SAR signal's polarization. This allows distinguishing between target orientations and different reflection types, as the SAR

Figure 2.2. An X-band SAR image measured by the German E-SAR airborne system in Finland. The black areas are lakes, the dark areas are fields, and the bright areas correspond to forests and buildings. Image size from left to right is 9.5 km.

signal polarization usually changes during reflection. SAR imaging and interpretation techniques that utilize polarization changes encompass a related scientific discipline called *polarimetry (PolSAR)*. In simple terms one can say that polarimetric SAR measurement yields more information about the structure of the object and the type of reflection from the object than does single polarization SAR. Polarimetry is used to improve image classification and target detection. Classification and visualization methods for polarimetric data are still under active development.

Another widely used technique in SAR remote sensing is *interferometry (InSAR)*. The coherent nature of the imaging signal allows combining images from several orbits and even from several instruments. With interferometry it is possible to combine two measurements from two parallel imaging tracks and measure the relative distance of targets from the measurement system with the help of a slowly varying phase difference map, called an *interferogram*. Interferometric techniques are widely used in terrain elevation model measurements and long term elevation change monitoring, where statistical techniques allow for the detection of elevation change trends on the order of one millimeter per year.

When polarimetry and interferometry are combined, the respective discipline is called *polarimetric interferometry (Pol-InSAR)*. This technique can distinguish between reflection types while determining also their elevation difference. This allows for example to distinguish ground reflection from volume scattering in forest remote sensing and calculate forest height. Determination of forest height by spaceborne SAR is under active development as it is potentially the most accurate method for global biomass estimation to date.

In this work both polarimetric and interferometric techniques are studied and developed further.

3. Development of analysis methods for fully polarimetric SAR images

This chapter concentrates on the development of a novel polarimetric SAR decomposition technique and the improvement of polarimetric SAR image visualization schemes. The chapter summarizes the work on alternative polarimetric parameters and polarimetric visualization, presented in Publication I. The first concepts of alternative parameters were published by the author in [45] and the work was continued in [46, 47]. The visualization techniques were developed in Publication I and in [48, 49].

The chapter is organized as follows: Section 3.1 describes the basic formalism of SAR polarimetry and gives an introduction to incoherent eigenvalue decomposition, describes alpha and entropy parameters and problems related to the usage of those parameters. In Section 3.2 it is shown, how the eigenvalue decomposition scheme can be improved by introducing the power normalized coherency matrix and using similarity invariants of the new matrix. Section 3.3 shows how the proposed decomposition parameters can be used to improve polarimetric image visualization schemes. Conclusions regarding the chapter are given in Section 3.4.

3.1 Polarimetric SAR

Polarization describes the oscillation plane of the electric field vector in a propagating electromagnetic wave. The electric field can either oscillate in a plane or draw an ellipse during its propagation; these polarization states are called linear or elliptical polarization, respectively, according to the pattern which is drawn by the tip of the electric field vector when inspecting the wave from the propagation direction. Polarization is described by the properties of this pattern; for example, the polarization of the wave can be horizontal, elliptical, or circular. During the scattering event, the polarization state of the electromagnetic wave usually changes.

Therefore radar systems often measure also polarization in order to extract some additional information about the scattering event.

3.1.1 Tools for polarimetric SAR image analysis

Many modern SAR systems, especially advanced airborne systems, possess a fully polarimetric capability and a growing number of applications can take advantage of fully polarimetric data. In fully polarimetric radar systems, transmitted and received wave polarization states are identified by measuring coherently the four (transmitted and received) polarization combinations in orthogonal pairs. The four measured complex parameters constitute the *scattering matrix* **S**, describing the transformation of the polarization of a wave, incident upon a scatterer $\vec{E}_i$, to the polarization of the scattered wave $\vec{E}_s$ as

$$\vec{E}_s = \begin{bmatrix} E_{ps} \\ E_{qs} \end{bmatrix} = \frac{e^{i\kappa R_t}}{R_t} \begin{bmatrix} S_{pp} & S_{pq} \\ S_{qp} & S_{qq} \end{bmatrix} \begin{bmatrix} E_{pi} \\ E_{qi} \end{bmatrix} = \frac{e^{i\kappa R_t}}{R_t} \mathbf{S} \vec{E}_i, \tag{3.1}$$

where $\kappa = 2\pi\lambda^{-1}$ is the wavenumber and R_t is the distance of the scatterer from the radar, and p and q denote polarization [39]. Note, that the polarization states are denoted in S_{pq} for both transmitted and received polarization in a orthogonal polarization basis, defined by the selected antenna system properties (The Backscattering Alignment convention [36] or antenna centric coordinate system is used here). Most common orthogonal polarization bases used in SAR systems are horizontal-vertical and left-right circular polarization combinations.

The scattering matrix **S** is a fundamental variable in SAR polarimetry. It describes fully the relation between the transmitted and received signal at any polarization. Each pixel of the polarimetric SAR image corresponds to a single scattering matrix which also yields information about the reflection. For example, when scattering matrix has ones on the main diagonal and zeros on the other diagonal, we can say that the reflection does not alter the transmitted polarization in any way and the reflection is probably a simple specular reflection. The scattering matrix is related to the power based radar cross section defined in (2.1) as [39]

$$\sigma_{pq} = 4\pi \left| S_{pq} \right|^2 . \tag{3.2}$$

When studying scattering from a field or forest, a single scattering matrix is not sufficient because of noise and variability. A single scattering

matrix becomes a statistical sample from a larger ensemble, described by a distribution function. In order to describe this underlying distribution, a *covariance matrix* can be used [39]. The covariance matrix is defined as an expected value of the product of the scattering vector $\vec{k}$ with its complex conjugate $\vec{k}^{\dagger}$:

$$\langle \mathbf{C} \rangle = \left\langle \vec{k}\vec{k}^{\dagger} \right\rangle . \tag{3.3}$$

Here $\langle ... \rangle$ operator denotes statistical averaging (in SAR polarimetry the averaging is usually done spatially) and † denotes the complex conjugate transpose. The scattering vector $\vec{k}$ can be formed from the measured scattering matrix elements, for example as

$$\vec{k} = [S_{HH}, S_{HV}, S_{VH}, S_{VV}] . \tag{3.4}$$

The scattering matrix elements can be used in a different order, in a different polarization basis and in linear combinations to form the measurement vector, however, the used basis has to remain orthogonal. The covariance matrix is by definition always a Hermitian (self-adjoint) matrix, i.e. a matrix which is equal to its conjugate transpose. Hermitian matrix diagonal elements are real and it has real eigenvalues: the eigenvectors form a unitary basis.

The covariance matrices in various bases have been used to describe the polarimetric measurement with many different names. For example, the Stokes matrix, which is widely used in optical polarimetry, is also a variation of the covariance matrix. Relations between different covariance matrices in polarimetry have been reviewed in Publication I. It is important to recall here that the averaged covariance matrix constitutes the standard deviation for the multivariate case; it is sufficient to describe statistically the measurement when measured variables follow a multivariate normal distribution. In the case of polarimetry, this applies only to homogeneous distributed targets.

3.1.2 Target decomposition techniques

The measured entity in polarimetry, the scattering matrix (3.1), consists of four complex numbers, which are not easily interpreted in terms of the scattering properties of the target. The scattering matrix can also be measured in several different orthogonal polarization coordinates, which complicates the interpretation further. For easier analysis it is often convenient to decompose the scattering matrix into simpler elements.

A simple example of scattering matrix decomposition, called Pauli decomposition, presents the scattering matrix (3.1) as a weighted sum of Pauli spin matrices similarly to

$$\begin{bmatrix} a+b & c-id \\ c+id & a-b \end{bmatrix} = a \begin{bmatrix} 1 & 0 \\ 0 & 1 \end{bmatrix} + b \begin{bmatrix} 1 & 0 \\ 0 & -1 \end{bmatrix} + c \begin{bmatrix} 0 & 1 \\ 1 & 0 \end{bmatrix} + d \begin{bmatrix} 0 & -i \\ i & 0 \end{bmatrix}. \quad (3.5)$$

When the Pauli matrices on the right hand side of (3.5) are interpreted as scattering matrices (in horizontal-vertical polarization basis), they can be interpreted as four reflection types distinguishable with polarimetric measurement. The target is therefore decomposed as

$$\text{Target} = \text{Surface} + \mathbf{0^0}\text{Dihedral} + \mathbf{45^0}\text{Dihedral} + \text{Antisymmetric} \quad (3.6)$$

and the weights a, b, c, d in (3.5) can therefore be interpreted as the weights of different scattering mechanism contributions. Pauli decomposition has also some other benefits. It appears that the last component in (3.5) is always zero for backscattering from reciprocal targets (most SAR measurements) and the first component is roll-invariant. Roll-invariance means that the variable is insensitive to SAR system attitude around the line of sight axis. This and similar decompositions belong to the class of so-called coherent decompositions.

Another type of decompositions deals with the second order statistics of polarimetric SAR data (the covariance matrix), providing valuable tools for understanding the underlying physical properties of backscattering from distributed targets. The decompositions can be also divided into mathematically motivated [5] and physics model based schemes [14, 15]. An overview of relevant decompositions is given in [8].

One of the most popular schemes, which belongs to incoherent class of decompositions was proposed by Cloude and Pottier [5, 8]. It is widely used in many PolSAR applications, e.g. land cover classification [9]. However, it appears to be computationally expensive due to eigenvalue calculation and does not provide straightforward physical interpretation of the scattering event. In the following sections the eigenvalue decomposition is reviewed and several improvements are suggested to both, the calculation efficiency and interpretation.

3.1.3 Incoherent eigenvector-eigenvalue decomposition

Incoherent eigenvalue based polarimetric target decomposition [5, 8] introduces elegant interpretation of the decomposition as an incoherent sum

of three orthogonal scattering mechanisms appearing with a certain probability proportional to the covariance matrix eigenvalues. In this decomposition the covariance matrix

$$\langle \mathbf{T} \rangle = \left\langle \vec{k}\vec{k}^{\dagger} \right\rangle \tag{3.7}$$

is formed from Pauli decomposed (3.5) scattering matrix elements and it is called *coherency matrix*. The coherency matrix is decomposed by means of eigenvectors k_n and eigenvalues λ_n as

$$\langle \mathbf{T} \rangle = \lambda_1 \vec{k}_1 \vec{k}_1^{\dagger} + \lambda_2 \vec{k}_2 \vec{k}_2^{\dagger} + \lambda_3 \vec{k}_3 \vec{k}_3^{\dagger}. \tag{3.8}$$

In matrix notation, decomposition of a Hermitian matrix $\mathbf{T}$ into its eigenvalues λ_n and eigenvectors k_n would be written as

$$\mathbf{T} = U \begin{bmatrix} \lambda_1 & 0 & 0 \\ 0 & \lambda_2 & 0 \\ 0 & 0 & \lambda_3 \end{bmatrix} U^{\dagger}, \tag{3.9}$$

where unitary rotation matrix U columns form three eigenvectors:

$$U = \begin{bmatrix} \vec{k}_1 & \vec{k}_2 & \vec{k}_3 \end{bmatrix} = \begin{bmatrix} \cos\alpha_1 & \cos\alpha_2 & \cos\alpha_3 \\ \sin\alpha_1 \cos\beta_1 e^{i\delta_1} & \sin\alpha_2 \cos\beta_2 e^{i\delta_2} & \sin\alpha_3 \cos\beta_3 e^{i\delta_3} \\ \sin\alpha_1 \sin\beta_1 e^{iz_1} & \sin\alpha_2 \sin\beta_2 e^{iz_2} & \sin\alpha_3 \sin\beta_3 e^{iz_3} \end{bmatrix}. \tag{3.10}$$

Parameters α_n, β_n, δ_n and z_n define eigenvector directions in relation to covariance matrix basis.

Qualitatively, the covariance matrix is interpreted as a incoherent sum of three orthogonal scattering mechanisms described by eigenvectors $\vec{k}_n$, appearing with probability p_n, described by eigenvalues λ_n as

$$p_n = \frac{\lambda_n}{\sum_{m=1}^{3} \lambda_m}. \tag{3.11}$$

Additionally to eigenvalues, Cloude and Pottier proposed some additional parameters for interpretation of the scattering event [9]. The first is target entropy, inspired by entropy from Shannon [63] information theory. For a distributed target where certain scattering mechanism $\vec{k}_n$ occurs with a probability p_n, the target entropy H is defined as

$$H = -\sum_{n=1}^{3} p_n \log_3 p_n. \tag{3.12}$$

The entropy describes polarimetric variability of the backscattering. When the target transforms the incident wave always in the same way, target entropy is lowest; if the target changes the polarization randomly, target entropy is maximal.

The second parameter was proposed to describe the way the polarization changes during the scattering process. The parameter is called average alpha angle ($\bar{\alpha}$) and it describes the average orientation of eigenvectors $\vec{k}_n$. It is defined as Bernoulli weighted average of eigenvector orientation angles [9] α_n, see rotation matrix (3.10), as

$$\bar{\alpha} = \sum_{n=1}^{3} p_n \alpha_n. \tag{3.13}$$

In this case $\bar{\alpha}$ has units of an angle and it is interpreted as an average scattering mechanism; for example if $\bar{\alpha} = 0$, the scattering is pure single bounce reflection.

The third parameter proposed to describe the scattering event, is the total backscattered power of the target. It is called *span* and it can be calculated as the trace of covariance matrix, it equals also to the sum of covariance matrix eigenvalues [5],

$$\text{span} = \lambda_1 + \lambda_2 + \lambda_3. \tag{3.14}$$

Span, entropy and average alpha angle are considered as the main polarimetric features of a scatterer [9]. However, entropy and $\bar{\alpha}$ are not independent variables. If target entropy is high, $\bar{\alpha}$ is restricted to a certain range of values which diminishes to a single point when entropy is equal to one, the highest value. Entropy H and $\bar{\alpha}$ have been widely used in SAR polarimetry [9, 31, 13].

Despite their simple interpretation, several drawbacks remain in the definition of these parameters. The $\bar{\alpha}$ definition as a weighted average of eigenvector angles from a certain direction in complex spherical coordinates makes its physical meaning obscure. The computation of both H and $\bar{\alpha}$ is also time-consuming, because it requires averaging and eigenvalue and eigenvector calculation for each pixel of a polarimetric image.

As demonstrated in Publication I similar information can be extracted from polarimetric SAR image without eigenvalue and eigenvector calculation.

3.2 Improved parameters for polarimetric SAR image analysis

As mentioned earlier, the covariance matrix properties can be divided into basis independent properties (like eigenvalues) and basis dependent properties (eigenvectors). When keeping in mind that all covariance matrices are similar and Hermitian, one can find additional matrix invariants

which are easier to calculate than eigenvalues. In Publication I it is shown that trace, determinant and square of Frobenius norm of covariance matrix:

$$\mathrm{trace}(\mathbf{C}) = \lambda_1 + \lambda_2 + \lambda_3, \tag{3.15}$$

$$\det(\mathbf{C}) = \lambda_1 \lambda_2 \lambda_3, \tag{3.16}$$

$$\|\mathbf{C}\|_{Fr}^2 = \lambda_1^2 + \lambda_2^2 + \lambda_3^2, \tag{3.17}$$

form an alternative set of invariant parameters and the three eigenvalues can be expressed as roots of a characteristic equation formed by those invariants,

$$\lambda^3 - \lambda^2 \mathrm{trace}(\mathbf{C}) + \frac{\lambda}{2}\left(\mathrm{trace}(\mathbf{C})^2 - \|\mathbf{C}\|_{Fr}^2\right) - \det(\mathbf{C}) = 0. \tag{3.18}$$

All three invariants are just simple linear combinations of matrix elements or squares of the elements and are easy to calculate.

Regardless of the basis of the scattering vector, covariance matrices share the same invariants because of their similarity. In SAR polarimetry this means that the Stokes matrix, Mueller matrix, coherency matrix, covariance matrix, covariance matrix in circular basis, etc., have the same eigenvalues, determinant, trace and squared Frobenius norm. Interpretation of these invariants in terms of polarimetry is discussed more deeply in Publication I. The first invariant, trace of the covariance matrix, has a simple meaning: it is the total backscattered power (3.14), often also called span.

In order to utilize those invariants with eigenvalue decomposition scheme, a new matrix is proposed in [46] and the idea is further developed in Publication I. When normalizing the covariance matrix with its trace, one gets a matrix, whose eigenvalues are directly weighted eigenvalues (3.11) of the covariance matrix . The new matrix is defined as

$$\mathbf{N} = \left\langle \vec{k}^{\dagger}\vec{k} \right\rangle^{-1} \left\langle \vec{k}\vec{k}^{\dagger} \right\rangle = \frac{\mathbf{T}}{\mathrm{trace}(\mathbf{T})} \tag{3.19}$$

and it is called *power normalized coherency matrix*. The covariance matrix normalized in the described way opens up several simple interpretation schemes.

3.2.1 Scattering diversity and other alternatives to target entropy

It is shown in Publication I that the squared Frobenius norm (3.17) of the normalized coherence matrix shares common features with target entropy. The Frobenius norm is also very closely related to root mean square

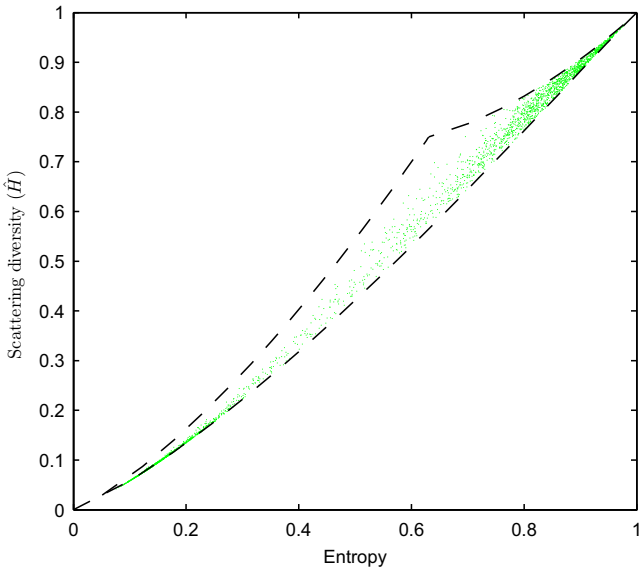

Figure 3.1. Relation between target entropy and scattering diversity ($\hat{H}$). The dots represent scatterplot between parameter values calculated for the San Francisco image, presented in Figure 3.5. The lines show extreme values of the parameters and conditions of these values in terms of eigenvalues. ©2009 IEEE.

of the eigenvalues, a classical measure of variability. It is shown in Publication I that the Frobenius norm of the normalized coherence matrix is a descriptor of the amount of power that one scattering mechanism represents from total power and it is called *specific scattering predominance*. The reciprocal of Frobenius norm of N gives an indicator of the number of scattering mechanisms present. In order to create a parameter similar to target entropy, the following parameter is defined in Publication I:

$$\hat{H} = \frac{3}{2}\left(1 - \|\mathbf{N}\|_{Fr}^2\right). \tag{3.20}$$

This parameter $\hat{H}$ is called *scattering diversity*. Figure 3.1 shows the relation between entropy and proposed scattering diversity, proving that both parameters are closely related and share therefore similar interpretation.

Also the determinant of the matrix N shares common properties with target entropy. It equals to zero for deterministic targets and has maximum value in the case of random target. The relation between entropy and the determinant of normalized coherence matrix is clearly non-linear, as shown in Figure 3.2.

However, as proposed in [46] and discussed in Publication I, the determinant of N can also be used to approximate the target entropy quite accurately.

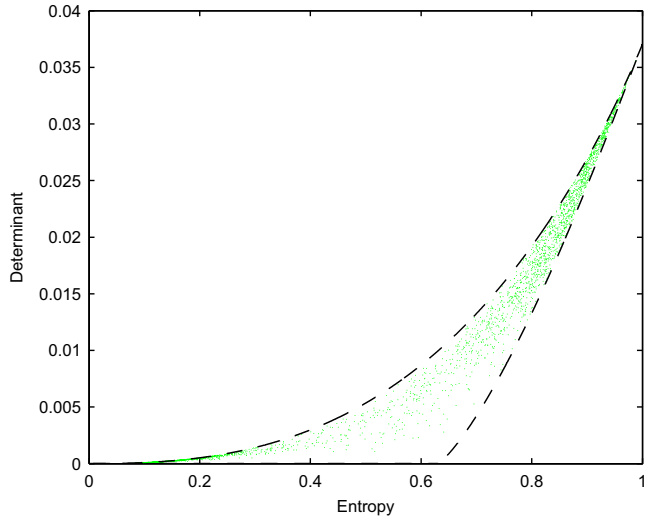

Figure 3.2. Relation between target entropy and determinant of N. Dots represent scatterplot between parameters values calculated for the San Francisco image, presented in Figure 3.5. The lines show extreme values of the parameters. Conditions for these values are same as in Figure 3.1. ©2009 IEEE.

By applying the Spectral shift theorem [25] to the matrix under determinant, an approximation for entropy can be developed. As shown in Publication I, approximation for entropy can be calculated as

$$H \approx H' = 0.78 \log_3(\det(\mathbf{N} + 0.16\mathbf{I})) + 2.52, \tag{3.21}$$

where $\mathbf{I}$ is an identity matrix.

The relation between entropy and approximated entropy is shown in Figure 3.3. The relation does not deviate much from linear, but calculation of H' does not involve any eigenvalue calculation, as the determinant of a matrix can be calculated as a simple linear combination of its elements.

3.2.2 Surface scattering fraction as an alternative to average alpha angle

Similarity invariants are independent of polarimetric basis and target orientation. However, polarization of the wave is an orientation related phenomenon which needs for full description also basis dependent parameters.

The coherency matrix was defined in (3.7) in such a way that one dimension is pointing to roll-invariant direction, which is a natural reference direction for the SAR imaging setup. The $\bar{\alpha}$ angle is a roll-invariant parameter, telling how far the scattering mechanism is from roll-invariant direction (single bounce scattering). By studying the power normalized

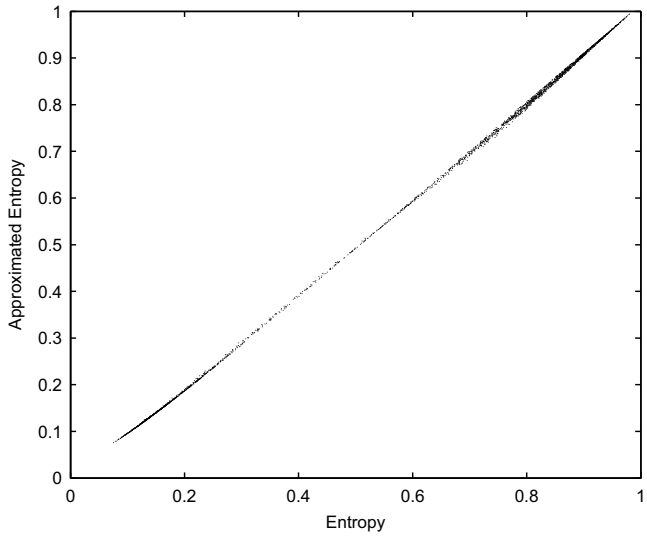

Figure 3.3. Scatterplot between target entropy (3.12) and target entropy calculated by approximation (3.21). ©2009 IEEE.

coherency matrix eigenvalue definitions stated in (3.9) and (3.10) one can see that the first element of N matrix is defined as

$$N_{11} = \sum_{n=1}^{3} p_n \cos^2 \alpha_n, \tag{3.22}$$

where p_n are matrix eigenvalues and α_n is the angle between eigenvector and the roll invariant scattering direction.

This relationship is similar to the definition of $\bar{\alpha}$ angle given in (3.13). It is easy to show that both $\bar{\alpha}$ and N_{11} depend on p_n and α_n through positive, monotonically increasing functions in the range $0 \leq \alpha \leq \pi/2$. On the other hand, by the definition of **N**, N_{11} can be written as

$$N_{11} = \frac{\left\langle |S_{HH} + S_{VV}|^2 \right\rangle}{\text{span}}. \tag{3.23}$$

The parameter can therefore be interpreted as a fraction of surface scattering (strictly speaking odd bounce scattering) from total backscattered power. It was first introduced in [46] and further developed in Publication I where the parameter was named *surface scattering fraction*. It can be shown that when the parameter has value 1, all backscattering comes from odd-bounce scattering; if the parameter has value 0, there is no odd-bounce scattering present. It can be also interpreted as a fraction of RL (right-left) polarized response from the total backscattered power in circular basis.

The surface scattering fraction is intuitive and very straightforward to calculate. Moreover, that definition is more clear and easier to understand

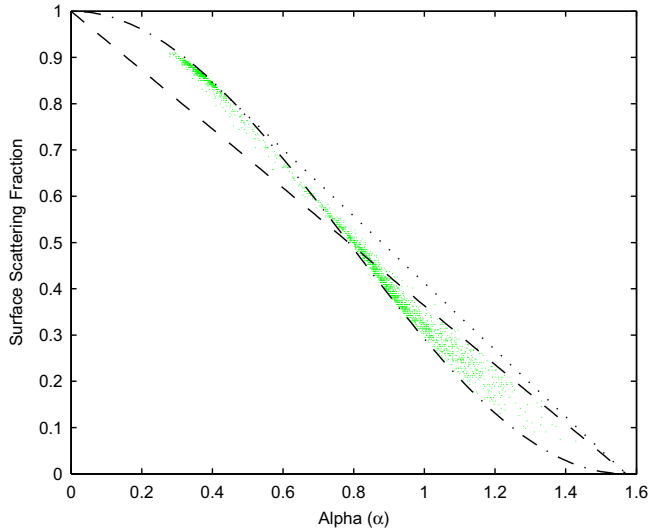

Figure 3.4. A scatterplot between average alpha (3.13) angle and surface scattering fraction (3.22). ©2009 IEEE.

than definition of $\bar{\alpha}$ (3.13). Information content of both parameters is similar, as shown in Figure 3.4, but proposed parameter is much easier to calculate as it does not need eigenvalue and eigenvector calculation. The definition of the surface scattering fraction (3.22) shows also that only part of the span-independent polarimetric information is described by the surface scattering fraction itself. The parameters N_{22} or N_{33} should additionally be used in order to gather all the information contained in the three eigenvectors. The surface scattering fraction idea can be expanded to another parameter, for example cross-polarized scattering fraction.

As discussed in Publication I, parameters from optical polarimetry or ellipsometry can give deeper insight to interpretation of polarimetric images. In the monostatic case, the optical linear retardance of a sample is representative of the anisotropy of the target's structure for non-deterministic targets, and it is related to the surface scattering fraction. The scattering diversity is directly connected to the depolarization coefficient in optical polarimetry.

3.2.3 Improved parameters in polarimetric SAR image classification

The scattering diversity (3.20) combined with the surface scattering fraction (3.22) form a target feature pair very similar to that of entropy and alpha angle. For example, they can be used to form a classification space

very similar to the well-known entropy-alpha classification scheme. As an example, a SAR image in Figure 3.5 (a) is classified with entropy-alpha classification scheme and the result is present in Figure 3.5 (b). The entropy-alpha classification space is shown in Figure 3.6 (a) with the same points presented also in the scattering diversity and surface scattering fraction space in Figure 3.6 (b). As it can be seen, the alternative parameter pair leads to a very similar result. The original classes separate well, but are slightly mixed near class borders. Both classification spaces are essentially the same, except that the entropy-alpha space is slightly differently curved.

However, it should be mentioned that both classifications have the following problems: the classification space is highly nonlinear and the class definitions do not have a strict physical background. Using the scattering diversity and the surface scattering fraction for classification does not overcome these shortages, but it improves calculation efficiency.

In Publication I it is proposed that the diagonal values of normalized coherency matrix; N_{11}, N_{22}, N_{33} could be directly used for classification. Because the sum of those three variables is constrained to one, the classical ternary diagram is easy to construct. The classification space can be interpreted through the three simple scattering mechanisms (the same as used in coherency matrix definition) in the three dimensional classification space, where all points lie on the surface determined by the constant sum constrain, as shown in Figure 3.7. In this diagram, the relative strengths of the three basic scattering mechanisms described by Pauli matrices can be represented unambiguously. The representation includes information about the entropy parameter in an intuitive way: the high entropy class is in the middle of the triangle and low entropy values lie on the edges. As the odd-bounce direction is roll-invariant, the corresponding class is clearly defined and is similar to the one in the entropy-alpha plot. Differences arise in double-bounce scattering, which can appear in different places depending on the orientation of the reflector.

From the presented classification results, a conclusion can be drawn that the eigenvectors are normally not far from the original axis, i.e. odd-bounce, even-bounce and cross-polarizer. This means that coherency matrix off-diagonal elements are often insignificant. Therefore classification by using just diagonal elements of the normalized coherency matrix gives results similar to those from eigenvalue based classification. For testing the significance of off-diagonal elements of the coherency matrix, a param-

(a) Total backscattered power.

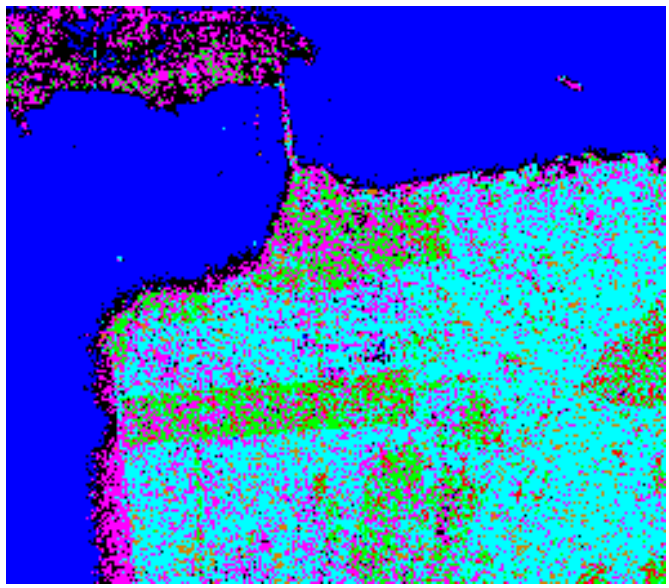

(b) Entropy-alpha classification.

Figure 3.5. Polarimetric AIRSAR image of San Fransisco Bay: (a) total power of backscattering, (b) result of polarimetric entropy-alpha classification. The classes in terms of entropy and alpha are given in Figure 3.6 (a).

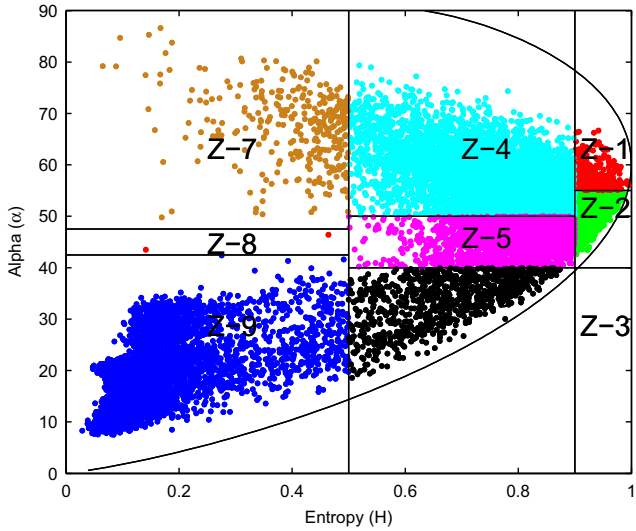

(a) Entropy-alpha classification space.

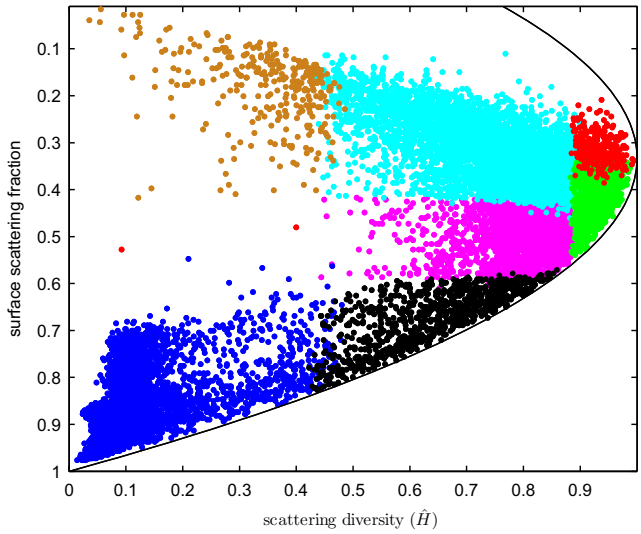

(b) Scattering diversity - surface scattering fraction classification space.

Figure 3.6. Polarimetric classification spaces: (a) well known entropy-alpha classification space with the San Francisco image classified according to the classification limits proposed in [8], (b) scattering diversity ($\hat{H}$) and surface scattering fraction (N_{11}) classification space, using the same data points and coloring as in (a). ©2009 IEEE.

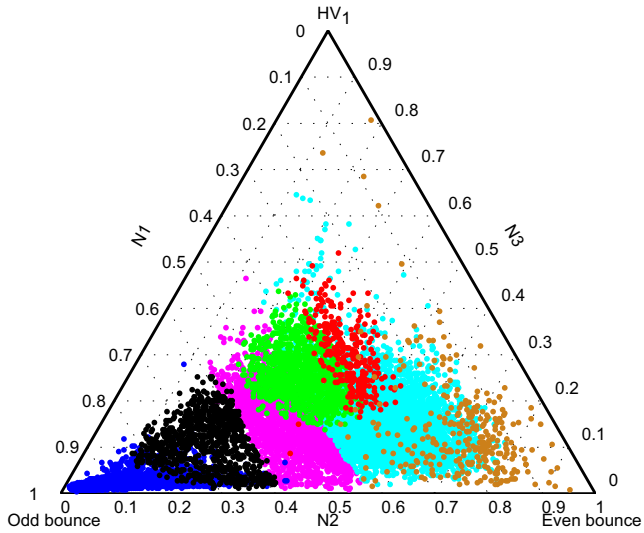

Figure 3.7. Polarimetric ternary diagram: classification space based N matrix main diagonal elements. A point in the diagram shows the relative strengths of the three basic scattering mechanisms described by Pauli matrices. The diagram shows all N_{11}, N_{22}, N_{33} combinations without overlap. Scattering diversity or entropy is lowest on the edges and highest in the center of the triangle where all scattering mechanisms have equal strength. Dots are colored according to entropy-alpha classification results presented in Figure 3.6. ©2009 IEEE.

eter where the sum of squared elements of coherency matrix off-diagonal elements is divided by the sum of squared elements of main-diagonal elements is proposed in Publication I. With this parameter the usefulness of eigenvalue decomposition for particular target can be evaluated.

3.3 Polarimetric image visualization

The polarimetric descriptors which are simple to calculate, open possibilities to take a step from classification schemes to visualization schemes. SAR image visualization can be treated also as a classification approach but, instead of discrete classes, continuous variables are presented as colors in image. There are several ways to visualize multivalued data for easier human perception. Usage of colors is just one way to do it. As visualization is not the main content of this this work, the topic will be covered briefly.

Human eye does not sense polarization and therefore there is no natural way to present polarization visually. Polarization states are often specified and most easily comprehended in terms of the polarization ellipse, which can be parametrized in several ways. Georg G. Stokes proposed in

1852 four parameters for description of polarized light [11]. The first parameter described intensity, second described degree of polarization and the last two described the polarization ellipse. There are four parameters for describing polarized radiation and only three color channels in color images, meaning that one cannot show all the polarization information in colors. However, when dealing with fully polarized light, the degree of polarization can be omitted and a single coherent wave polarization state could in principle be mapped to color unambiguously.

However, PolSAR image contains, additionally to received wave polarization, also the transmitted wave polarization. Therefore, there are always more variables in a single polarimetric SAR image pixel than can be visualized in a color image. Due to this fact, it is not probable that a single visualization scheme would be established in the future; rather, there will always be multiple ways to visualize a PolSAR image. In [49] a general framework of color visualization along with color model connections to polarized wave representation models were discussed.

3.3.1 Color models

In order to present any numerical data in color, one needs a color model. The color model is a mathematical representation which converts numbers into colors. The first known color system comes from Finland. Sigfridus Aronus Forsius presented in his book *Physica* a circular color system in 1610 [26]. The first well known scientific color model was developed by Isaac Newton in 1666 [26]. The Newton color wheel was improved by Moses Harris who added color shades and in 1810 Philipp Otto Runge introduced saturation into his color map where all colors were mapped to the sphere [26]. After Thomas Young and Hermann von Helmholtz presented the idea of trichromatic color vision [26], James Clerck Maxwell experimented with colors and proposed first color matching functions based on three primary colors; red, green and blue [26]. He also arranged primary colors additively within a triangle, nowadays known as the Maxwell color triangle, which was a precursor to modern CIE (International Commission on Illumination) color models [26]. The Maxwell color model is shown in Figure 3.8. The sum of equal portions of base colors is always white and in the ternary plot the sum of three variables is also constant. Note that the Maxwell color triangle is very similar to a ternary plot in Figure 3.7.

Most modern color systems are based on three parameters, because the

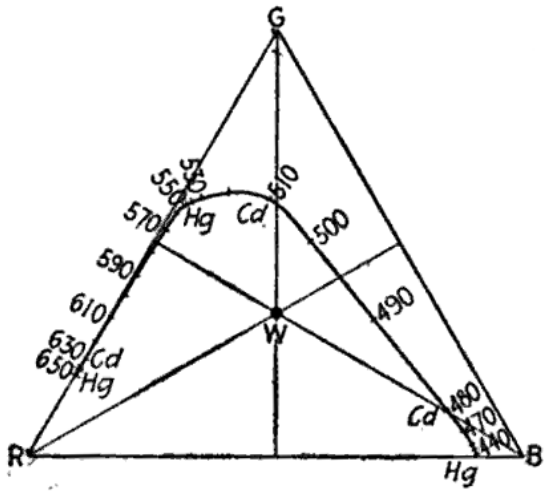

Figure 3.8. Maxwell color triangle, a color model which uses ternary plot principle to map three main colors. Letters R, G, B and W denote red, green, blue and white color, respectively. The numbers denote wavelengths of light. Picture from [35].

human color vision is trichromatic. The color systems can be divided into two broad approaches. The parameter triplet is either based on direct sensory input values, or the triplet tries to mimic human comprehension of colors. The first approach operates with the intensity of red, green and blue color in Cartesian coordinates, another maps color values to cylindrical or spherical coordinate system to get perceptually more relevant parameters like hue, saturation, lightness etc. In Cartesian coordinates parameters are linear, but in cylindrical or spherical systems some parameters are periodic, for example hue. Perceptual parameters are also often interconnected; for example, if the overall intensity is zero, the hue or saturation has no values [26].

There are many similarities between color models and polarization visualization models, for example the similarity between Poincaré sphere and Runge's color sphere [26]. As with the color models, it can be also seen here that by changing the coordinates from Cartesian coordinates into spherical coordinates, periodic parameters are formed which are often easier to comprehend.

3.3.2 Polarimetric SAR image visualization with colors

Polarimetric information in SAR images has been visualized in numerous ways. Currently two representations are commonly used; direct polari-

metric red-green-blue (RGB) mapping and synoptic representation [24]. In the simple RGB approach polarization channel intensities are mapped to red, green and blue color intensities. This method allows to show three polarimetric channels in a single color image. The method is fast, but the color scale varies from one image to another and colors have slightly different meaning in different images. The synoptic representation (alpha-entropy-span HSI mapping) is a much more elaborated approach with elegant interpretation. Unfortunately the parameters require more processing time and the resulting image has lower resolution than the original due to the averaging needed for entropy and $\bar{\alpha}$ calculation.

In [48] it was proposed by the author that intensity and hue layers of the HSI image can be presented with a resolution which is higher than that of the saturation layer. This can be applied only in cylindrical color models, where different color parameters have different nature, but cannot be applied in RGB models. Calculation of the scattering diversity needs always some averaging, thus the corresponding image is in lower resolution. However, when the image is accompanied with high resolution intensity layer (as is done in optical image pansharpening), all the details can be preserved for visual interpretation with only minor image artifacts as shown in Figure 3.9.

In order to achieve good visualization results in the case of polarimetric SAR image, the color model should be selected according to the image parameters one wants to represent. Linear parameters should be presented in RGB color space and the parameter balance point (white color) should have a special meaning if possible. Periodic variables should be presented in cylindrical color models together with linear parameters corresponding to intensity and saturation. As there are more polarimetric parameters than can be presented in a single image, there will always be several representations for different needs. It is important to select the most relevant parameters for the case.

In order to ease the parameter selection one can classify purely polarization related parameters in roughly three classes [10]. The first one is connected to the change of phase of the eigenpolarization states, the second one is connected to the change of amplitudes of the eigenpolarization states and the third one is linked to the depolarization properties of the target. Additionally the scattering intensity is needed. Each of these classes can be connected to the color space variable class which is the most suitable for visualization. Phase change related parameters are

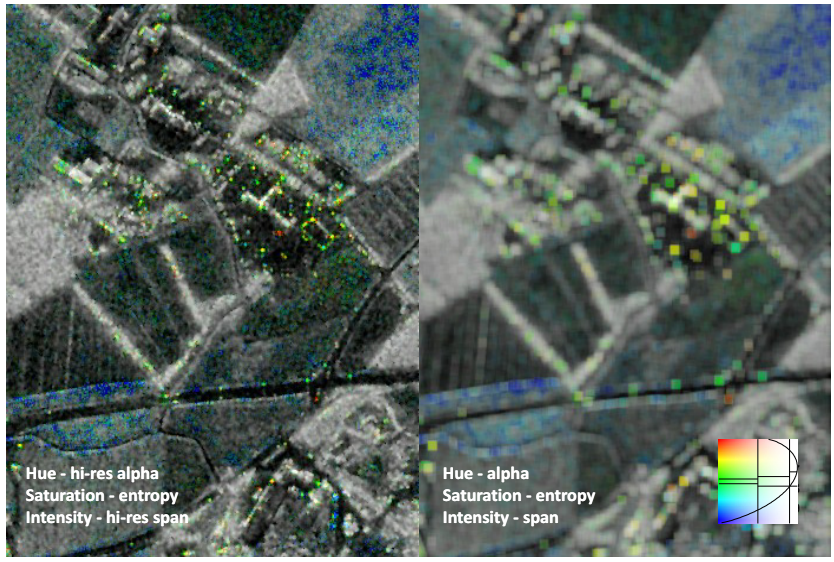

Figure 3.9. Image clarity improvement by introduction of multiresolution approach to synoptic visualization scheme. On the right is shown a synoptic HSI visualization of a polarimetric SAR image where average alpha, span and entropy are used. All parameters are spatially averaged for eigenvalue calculation. On the left is the visualization scheme proposed in [48] where $\bar{\alpha}$ and span on hue and intensity layers are presented in full resolution and only entropy is in lower resolution as it is averaged for calculation.

suitable for presenting with periodic color variables, polarization amplitude related parameters can be presented with both periodic and linear parameters, and depolarization related parameters are best to map to parameters which control also periodic variable, for example saturation or lightness. Scattering intensity is easy to connect to image intensity. In the following some examples of visualization schemes based on normalized covariance matrix approach are given.

3.3.3 Polarimetric SAR image visualization using parameters based on normalized coherency matrix

As mentioned earlier, easily computable polarimetric descriptors proposed in Publication I are handy in SAR image interpretation and visualization schemes. Two examples of visualization schemes are discussed here. The first one arises from similarity of the ternary plot and Maxwell color triangle and uses normalized covariance matrix main diagonal elements. Three linear variables indicate that the RGB model should be used. When arranging the power of basic scattering components (coherency matrix main diagonal components) to Maxwell color triangle, every corner represents a pure scattering mechanism and in the middle of the triangle

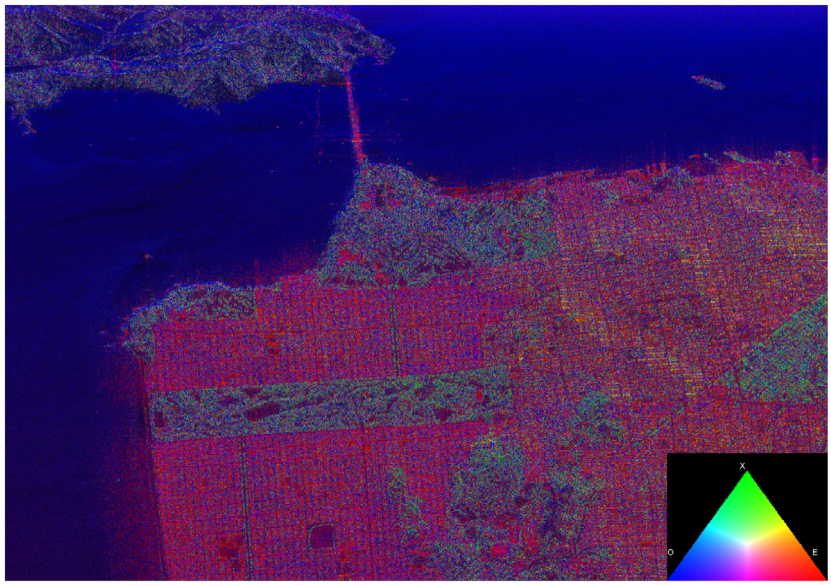

Figure 3.10. Fully polarimetric SAR (AIRSAR) image of San Francisco Bay presented by using Maxwell color triangle inspired color map. The color of a pixel is determined by relative strength of basic scatterers represented by Pauli matrices (N_{11}, N_{22}, N_{33}) as shown in the diagram in the lower right. The letters denote three pure scattering mechanism, odd bounce (O), even bounce (E) and cross-polarizer (X). The intensity of a pixel is determined by logarithm of total backscattered power (span).

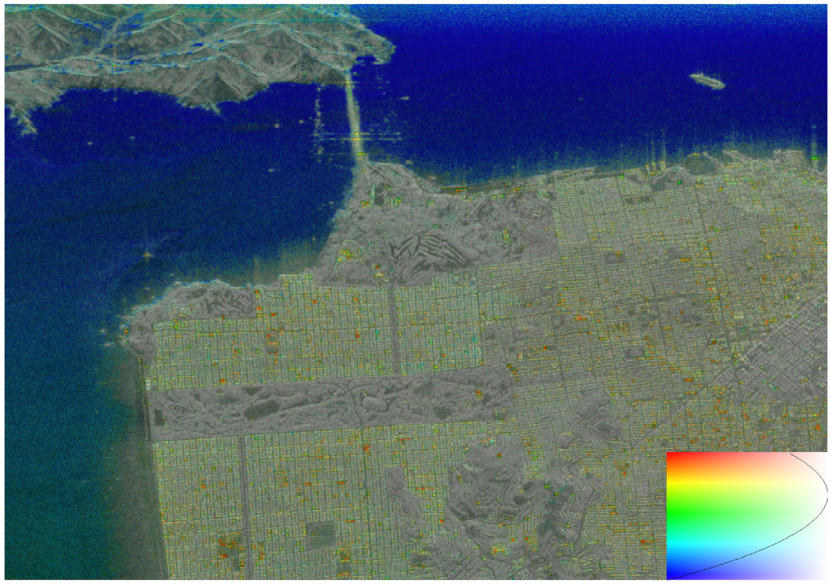

Figure 3.11. Fully polarimetric SAR (AIRSAR) image of San Francisco Bay in multiresolution-synoptic visualization, where hue is described by surface scattering fraction, saturation by scattering diversity and intensity by $\log(\text{span})$. Span and surface scattering fraction are averaged over a 4x4 window and scattering diversity over a 20×20 window. Gray denotes areas, where polarimetric information is random (parks and forest), blue denotes single-bounce scattering and red double-bounce scattering.

all scattering mechanisms are equiprobable and the color is white. The example of this visualization scheme is presented in Figure 3.10. Single bounce scattering from the sea is blue, double bounces from urban areas appear red and cross-polarization response from forest is green. A similar visualization scheme can be applied also for eigenvalues.

Another example can be constructed by using scattering diversity and surface scattering fraction, see Publication I. The scattering diversity tells whether it is possible to identify a single coherent scattering mechanism responsible for most of the reflection. This parameter is similar to the polarization degree and it can be used as saturation of the color in visualization. The surface scattering fraction tells the fraction of received power reflected back by a roll invariant single bounce reflection. When the parameter is equal to 1, all backscattering comes from odd-bounce scattering; if the parameter is equal to 0, there is no odd-bounce scattering present. This parameter belongs to the phase changing parameter class and suits well for use as a periodic color variable, such as hue. In this case the cylindrical HSI color model should be used. The visualization scheme was proposed for the first time in [24] and it was developed further in [48]. Figure 3.11 presents a polarimetric AIRSAR image in HSI representation. Sea appears blue, buildings appear green and red, and forest is gray. The forest has gray color because color saturation is low when scattering mechanism is random. This approach benefits from averaging of scattering diversity parameter and noise in polarimetric information content, compared to the previous approach, is reduced. However, averaging brings an additional step to calculations.

3.4 Conclusions of the chapter

In this chapter, a short overview of polarimetric SAR image analysis with the covariance matrix decomposition was given. It was shown that the eigenvalue decomposition of covariance matrix is a powerful tool in polarimetry, providing a sound framework for understanding of the scattering event. The study of covariance matrix invariance and symmetry properties led to the definition of alternative parameters and interpretations. It was shown that the eigenvalue decomposition parameter calculation can be simplified and interpretation can be broadened by introducing power normalized coherency matrix.

Instead of entropy, *scattering diversity* or *specific scattering predomi-*

nance can be used and the $\bar{\alpha}$ can be replaced by *surface scattering fraction*. The proposed parameters are suitable for image interpretation, classification and visualization in a similar manner but are easier to calculate and comprehend and as they do not require calculation of eigenvalues or eigenvectors of the coherency matrix. The presented analysis gives a fresh insight to the interpretation of eigenvalue analysis based parameters and expectantly motivates SAR community to search connections between various approaches in polarimetry.

Polarimetric image visualization was discussed in the second part of the chapter. Optimal visualization of multi channel SAR data is a subject, which has not been very much studied. As it was shown here by the brief analysis, there are many ways to present polarimetric data and some ways are more justified than others. Based on color models and polarimetric parameters similarities some general principles for polarimetric image visualization were provided here. The proposed approach should help to find the most suitable match between the color model and polarimetric parameter set to achieve better results in image interpretation. The proposed visualization schemes are suitable for quick browsing and visual interpretation of large polarimetric SAR images. In future work, proposed and also other visualization schemes should be compared with each other quantitatively to find out the optimal visualization for further use.

The presented approach is one of many possibilities to use and understand information content in polarimetric SAR images. The backscattering from forested areas is polarimetrically very diverse. As forest is random medium for microwaves, a significant part of the polarimetric signal is noise. Usage of proper visualization schemes should help greatly to evaluate polarimetric information content in SAR images and isolate useful features for forest remote sensing.

4. Applications of polarimetric interferometric techniques for boreal forest remote sensing

This chapter concentrates on forest parameter retrieval in the boreal zone by various means of interferometry and polarimetric interferometry with L- and X-band airborne SAR systems. The work summarized here is published in Publication II, in Publication III and in [50, 52, 54, 51, 53].

Forest biomass is a key parameter of the global biosphere [41, 65]. Modeling addressing climate, ecology, and economics as well as many other prediction frameworks require an accurate assessment of global forest biomass [62]. Many different methods are used to produce accurate estimates of the desired parameter and airborne and spaceborne SAR is one of the tools that holds most potential for large scale mapping [29].

Already during the early days of SAR remote sensing, it was noted that the backscattered signal from a young forest is weaker than the signal from a taller and older forest [64]. A link between forest biomass and the backscattering coefficient was soon established and utilized in biomass mapping. However, the relation between a simple backscattering coefficient and the forest biomass is sensitive to imaging conditions, includes large errors and most of all, saturates for already relatively low biomass values [12]. Therefore, the scientific community has been searching for more accurate means to measure forest parameters by utilizing more advanced SAR imaging and analyzing techniques.

This work contributes to the development of SAR based methods to measure forest height from airborne and spaceborne systems. Tree height, or more precisely tree stem length, is related to tree biomass through allometry equations [74] and therefore forest height measurement allows the creation of rather accurate biomass maps.

This chapter is organized as follows: Section 4.1 provides a short introduction to forest height calculation with the Random Volume over Ground (RVoG) model and interferometric SAR measurement techniques. Sec-

tion 4.2 describes the material used in this work. Section 4.3.3 describes, how RVoG model inversion for tree height retrieval was demonstrated for the first time for a boreal forest. In Section 4.4 the interferometric phase center location is studied and a new inversion method for the RVoG model and an auxiliary ground model is proposed and demonstrated. The method opens up the possibility to produce accurate forest biomass estimate maps from spaceborne X-band images. Finally, conclusions of the chapter are summarized in Section 4.6.

4.1 Polarimetric and interferometric SAR techniques for forest height retrieval

As alredy mentioned, forest biomass can be estimated from ordinary SAR images, but simple backscattering coefficient based methods are inaccurate and saturate at higher levels of forest biomass. Recently significant progress has been made concerning retrieval of forest height, which is an important forest biomass related parameter by means of SAR interferometric and polarimetric interferometric techniques [71, 40], Publication II.

The SAR community usually denotes the term forest height as the distance between the ground and the top of the canopy layer. This term does not coincide in an exact way with any tree height related parameter used in forestry, like stem length or average height. The term comes from simplified scattering models where the forest is described as a layer of random scatterers and is meant to indicate the thickness of the idealized forest layer. As the resolution of SAR systems is usually lower than that of optical systems, the usage of a simple forest height concept is justified. The forest height attempts to describe the canopy height and is probably most closely related to dominant height, which in forestry describes the mean height of the dominant trees in a stand.

A number of established forest height retrieval techniques rely on model-based interferometric SAR (InSAR) analysis. While traditional coherent forward models [68, 32, 66, 33, 34, 72] provide a good insight into the expected behavior of the forest canopies, they require many input parameters and can seldom be inverted in practice due to the lack of measured observables. Common methods to overcome this difficulty include; increasing the number of independent observations through multi-polarization, multi-frequency, multi-incidence-angle and multi-baseline

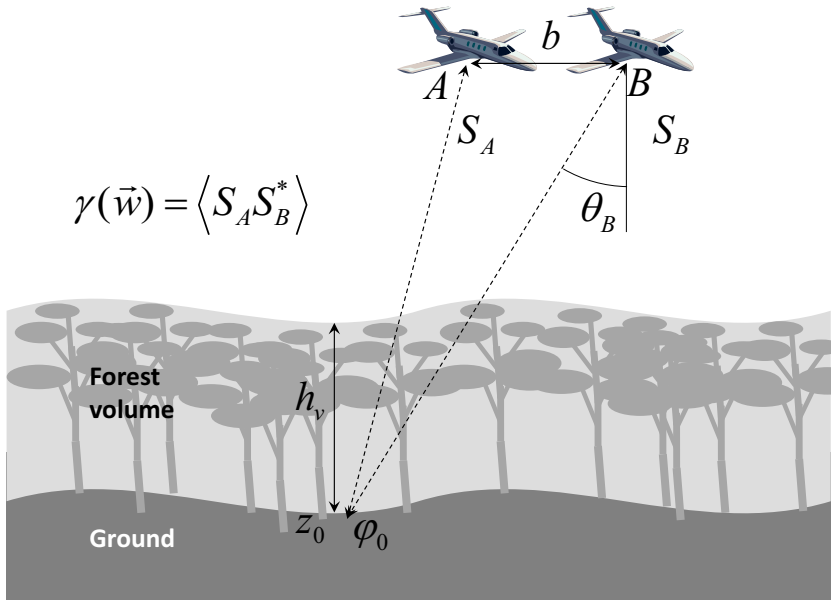

Figure 4.1. Polarimetric interferometric measurement for forest height estimation. Two measurements S_A and S_B are performed with two antennas, separated by baseline b. Measured complex coherence γ depends on polarization $\vec{w}$ which allows to calculate the height difference h_v between reflection from the ground and from the volume formed from trunks and branches.

acquisitions [70, 69]. The only drawback of these methods is the large amount of required measurements and auxiliary parameters which are rarely available in operational measurement situations.

The number of free parameters can also be reduced by using simpler models for data interpretation; however, these models still need to be capable of providing essential information about canopy properties. One relatively simple model which has shown good agreement with measurements is the Random Volume over Ground (RVoG) model [71, 70, 7, 2]. In the current work, the RVoG model has been used as a general framework to retrieve forest parameters from interferometric and polarimetric L- and X-band SAR measurements. In the next section, the model is presented in more detail.

4.1.1 Random Volume over Ground (RVoG) model

The RVoG model [71, 70, 7, 2] connects measured polarimetric interferometric coherence γ with key properties of the forest layer. The complex coherence of interferometric measurement is defined as the complex conjugate product of two SAR measurements, S_A and S_B, acquired from lo-

cations A and B separated by baseline b, see Figure 4.1. The coherence is dependent on the measurement polarization $\vec{w}$ and it is calculated for an ensemble of measurements as

$$\tilde{\gamma}(\vec{w}) = \left\langle S_A S_B^{\dagger} \right\rangle . \tag{4.1}$$

The RVoG model describes the vegetation layer (leaves + branches + trunks) as a homogeneous random medium of a given thickness located over an impenetrable ground. The ground reflection depends on polarization whereas the volume introduces an extinction and decorrelation of the signal. For a given spatial baseline the model produces an interferometric complex coherence $\tilde{\gamma}_m$ estimate that is a function of the polarization $\vec{w}$ and forest layer properties as [7]

$$\tilde{\gamma}_m(\vec{w}) = \exp(i\phi_0)\frac{\tilde{\gamma}_v + M(\vec{w})}{1 + M(\vec{w})}, \tag{4.2}$$

where $\phi_0 = \kappa_z z_0$ is the phase related to the ground topography z_0, and κ_z is the effective vertical interferometric wavenumber. Here $\tilde{\gamma}_v$ is volume induced coherence and M is the effective ground-to-volume amplitude ratio accounting for the attenuation through the volume:

$$M(\vec{w}) = \frac{m_G(\vec{w})}{m_v(\vec{w})} \exp\left(-\frac{2\sigma_v h_v}{\cos\theta_0}\right), \tag{4.3}$$

where m_G and m_v are ground and volume scattering amplitudes, σ_v is the mean extinction coefficient of the volume layer, h_v is the thickness of the volume layer and θ_0 is the mean incidence angle. Volume decorrelation for the vegetation layer without ground is given by [7]

$$\tilde{\gamma}_v = \frac{\int_0^{h_v} \exp\left(\frac{2\sigma_v z'}{\cos\theta_0}\right) \exp\left(i\kappa_z z'\right) dz'}{\int_0^{h_v} \exp\left(\frac{2\sigma_v z'}{\cos\theta_0}\right) dz'}. \tag{4.4}$$

The RVoG model performance has been assessed through theoretical studies and extensively demonstrated in various airborne SAR experiments in different forest environments ranging from tropical rainforest [69, 2, 19] and temperate broad-leaved forests [38] to boreal forests [73, 1, 16], Publication III, mostly at the X-, C-, and L-bands, as well as at longer wavelengths [17, 18]. Inversion of the RVoG model is applicable only to Pol-InSAR data since for single polarization InSAR the inversion problem becomes under-determined. However, under some simplifications or with the existence of additional information, the RVoG model can be successfully utilized even with single polarization channel data. Common simplifications to make the RVoG model invertible include the use of an external

ground digital elevation model (DEM), fixing the forest extinction coefficient to a certain value [19], Publication III, and, at higher frequencies, even discarding the ground scattering contribution [19] due to the high attenuation in the vegetation layer.

4.1.2 RVoG model in simplified form

The RVoG model is used in this work in a slightly rearranged form, first proposed by the author in [52]. The model (4.2) can be written in the form where its linear nature in the complex plane is easier to comprehend as follows:

$$\tilde{\gamma}(\vec{w}) = e^{(i\phi_0)} \left[(\gamma_V - 1)(1 + M(\vec{w}) e^{h_v \sigma_m})^{-1} + 1 \right]. \tag{4.5}$$

Here h_v is the height of the volume layer, ϕ_0 is the interferometric phase at the ground level, M is ground-to-volume amplitude ratio (4.3), and γ_V is coherence caused only by volume and is defined as

$$\gamma_V = \frac{e^{h(\sigma_m + i\kappa_z)} - 1}{(1 + i\kappa_z \sigma_m^{-1})(e^{h_v \sigma_m} - 1)}. \tag{4.6}$$

where κ_z is the vertical wavenumber. Local extinction $\sigma_m = 2\sigma_v / \cos\theta$ is defined by mean extinction σ_v and the local incidence angle θ. This form helps to locate simple model inversion cases, for example when retrieving extinction values of the forest [52].

By assuming the ground-to-volume ratio M to be 0 and extinction $\sigma_v = 0$, (4.5) can be simplified to

$$(\phi_\gamma - \phi_0) = sinc^{-1}|\gamma|, \tag{4.7}$$

which is often called the "sinc" approximation [6]. The approximation states that in the case of low attenuation and no ground reflection, scattering height in a forest is a $sinc^{-1}$ function of the coherence amplitude. This relation has been used for retrieving forest height from only coherence magnitude data [37, 6]. Another interesting relationship which can be derived by rearranging (4.5) and taking the argument of both sides,

$$arg\left(|\gamma| \, e^{i(\phi_\gamma - \phi_0)} - 1 \right) = arg\left(\gamma_V - 1 \right). \tag{4.8}$$

Thus, the M parameter can be eliminated from (4.5) and the inversion process becomes much simpler. (4.8) has two knowns, $|\gamma|$, ϕ_γ and three unknowns h_v, ϕ_0, σ_m. By knowing one parameter, inversion for the the other two parameters is possible. This equation can be used as a simple check to verify that the parameters are within a feasible range before model inversion is performed, or, it can be also used for model inversion as is done in [52].

Figure 4.2. Airborne instruments used in FINSAR measurement campaign. Left: E-SAR on board of Dornier airplane. Right: HUTSCAT scatterometer on board Bell JetRanger helicopter. Photos courtesy DLR and Aalto University.

4.2 Material of FINSAR airborne campaign

The material used in this work was collected mainly during the FINSAR airborne campaign, carried out jointly by DLR and TKK during the autumn of 2003 in Finland, see Publication II for details. The main instruments of the campaign were the German E-SAR system and the Finnish HUTSCAT ranging scatterometer, see Figure 4.2. Part of the test site was also covered later by laser scanning, providing accurate ground elevation and tree height measurements.

4.2.1 Test site

The FINSAR test site is located in southern Finland (N 60^0 $11'$, E 24^0 $29'$), in Kirkkonummi, near Helsinki. The area represents a typical land use scenario for southern Finland, where agricultural fields alternate with forest patches and lakes. The forest in the test area is heterogeneous and consists of rather small stands. The test area incorporates young and old coniferous stands and mixed (coniferous/deciduous) stands, clear-cuts, and mires. The dominant tree species are Scotch pine, Norwegian spruce, birch and alder. The terrain is relatively rough and rocky, especially in the forest. During the campaign deciduous trees were still in full leaf, but discoloration had already begun for the broad-leaved species.

4.2.2 E-SAR measurements

The E-SAR flight took place on September 29, 2003 between eight and nine o'clock in the morning. The instrument flew at an altitude of about 3 km along five parallel tracks, each separated by a spatial baseline of 5 m, and collected repeat pass quad-pol images at L-band (1.3 GHz) and

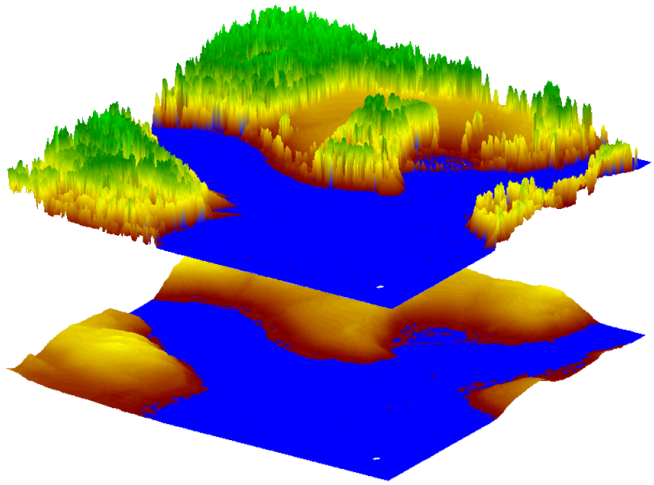

Figure 4.3. LIDAR measured digital elevation model (DEM) and canopy height model (CHM). The blue area in the front is a lake.

along a single track in a single-pass single-pol (VV) interferometric mode at X-band (9.6 GHz). The temporal baseline between subsequent tracks was approximately 12 - 14 minutes. Figure 2.2 shows an X-band E-SAR image measured during the FINSAR campaign. The weather during the image acquisition was, according to the weather station located in the area, mostly calm with almost no wind. Air temperature in the forest was around 10^0 C.

4.2.3 HUTSCAT measurements

Reference forest height and backscattering data were collected by the helicopter-borne HUTSCAT scatterometer [21], which is able to collect a vertical backscattering profile along the flight track at C-band (5.4 GHz) and X-band (9.8 GHz). Due to thick fog at the airport on September 29, the HUTSCAT measurement was carried out two days after the E-SAR measurements. HUTSCAT measured 11 transects, altogether 36 km. Most of the HUTSCAT measurements were concentrated on a 2 km $\times$ 2 km area (see Figure 4.4), covering the E-SAR near and mid range.

4.2.4 LIDAR measurements

LIDAR scanning over part of the FINSAR test site was performed on July 25, 2005 using the laser scanner Optech ALTM 3100 unit at a 1 km flight altitude. This provided a target point density of 3-4 pts/m^2. A digital elevation model (DEM) relevant to treetops was obtained by taking the

highest point within a 1 m grid, with missing points interpolated by Delaunay triangulation. Furthermore, the canopy height model (CHM) was obtained by simply subtracting the ground DEM from the corresponding treetop DEM. Information regarding individual tree heights can be derived from CHM using methods discussed in [23]. Part of the measured elevation model from the test site is shown in Figure 4.3.

4.2.5 Ground measurements and supplementary material

Ground measurements were made both on the E-SAR and HUTSCAT flight days. The test plots were located along the HUTSCAT flight lines. Soil moisture, temperature and leaf area index were measured and digital photographs were taken. Weather information was collected by two portable weather stations. Forest inventory data were made available by the local forest authority for the 136 ha area. An aerial image mosaic and maps are available for the whole test site.

4.3 Forest height estimation from L- and X-band E-SAR images using RVoG model inversion

This section summarizes the novel work related to forest height retrieval by means of polarimetric interferometry and RVoG model inversion for a boreal forest. The results were published in [50] and Publication II. Reference forest height measurements were made by the HUTSCAT scatterometer and the forest height was retrieved by the full RVoG model inversion for L-band interferometric measurements. Additionally, experimental restricted RVoG model inversion was applied for X-band single polarization interferometric measurement. The X-band forest height measurement capability was demonstrated for the first time. The correlation between HUTSCAT and ESAR height estimates (R=0.77 at L-band and R=0.75 at X-band) confirms the good agreement between the results obtained by the two approaches.

4.3.1 RVoG model inversion with E-SAR measurements

The estimation of forest height from interferometric coherence measurements is based on the inversion of the RVoG scattering model (4.2) by using in principle the three stage inversion process described in [7]. Assuming that all decorrelation is caused by volume decorrelation and ne-

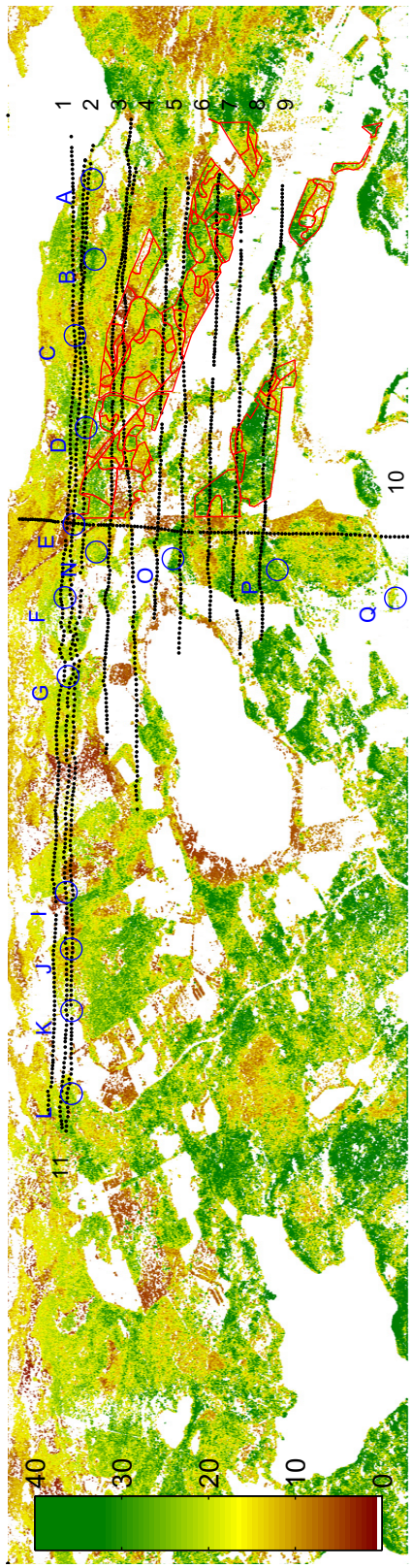

Figure 4.4. Forest height (m) map, generated by RVoG model inversion by using L-band Pol-InSAR complemented with an ancillary data acquisition map. The image is in SAR slant range geometry, the near range is at the top and far range at the bottom. The black dotted lines are the HUTSCAT flight tracks, the red lines show forest stand map (where available), and the blue circles mark ground measurement areas. The white regions correspond to unforested areas, such as lakes and fields. Image size from left to right is 9.5 km. ©2007 IEEE.

glecting other decorrelation sources (temporal, signal to noise ratio (SNR), and/or processing induced decorrelation contributions) the inversion problem (4.2) can be written in terms of a minimization problem between measured coherence $\tilde{\gamma}$ and modeled coherence $\tilde{\gamma}_m$ as

$$\min_{h_v,\sigma_v,m(\vec{w}),\phi_0} \|\tilde{\gamma}(\vec{w}) - \tilde{\gamma}_m(h_V,\sigma_v,m(\vec{w}),\phi_0)\| \,. \tag{4.9}$$

Note that the terms inside the brackets indicate the four unknowns. The problem can be solved uniquely in terms of a quad-pol single baseline acquisition [40] that provides three independent polarizations.

The quad-pol L-band 10 m nominal spatial baseline (corresponding to a nominal $\kappa_z = 0.11$) acquisition was chosen for the inversion, since it provides the best inversion performance in terms of vertical wavenumber.

In addition, the single-pass single-pol X-band acquisition was used for height inversion, as proposed in [27]. The inversion problem of (4.2) is underdetermined for a single baseline single-pol observation space, where only two observables are available to recover four unknowns. Nevertheless, a determined problem can be enforced by neglecting the ground scattering component and fixing the extinction coefficient. When fixing the value of the extinction coefficient σ_v ($\sigma_{v0} = 0.1$ dB/m in this study), assuming no ground contribution ($M = 0$) for all the polarizations and ignoring the ground phase ϕ_0, the inversion problem can be reduced to a single (real) parameter problem

$$\min_{h_v} \left\| \quad |\tilde{\gamma}(\vec{w})| - |\tilde{\gamma}_m(h_v,\phi_0|\sigma_v = \sigma_{v0})| \quad \right\| . \tag{4.10}$$

In this case the X-band height estimate is based solely on coherence amplitude. The forest mask needed for inversion, was generated by using L-band images and the SNR decorrelation method [20].

4.3.2 Forest height estimation from HUTSCAT backscattering profiles

In order to extract forest canopy height information from scatterometer measurements, the HUTSCAT measured vertical backscattering profile data were linked to the GPS measurements. Forest height was determined from the scattering profiles as the difference between tree top reflection and ground reflection with a tailored pattern recognition algorithm, designed as a part of this work. The algorithm was applied for both X-band and C-band-profiles. HUTSCAT data collection provided ≈ 32000 measurements along 11 transects, comprising ≈ 24000 height estimates calculated separately for X-band C-band.

4.3.3 Comparison of E-SAR tree height estimates with HUTSCAT estimates

The forest height map derived from E-SAR L-band fully polarimetric measurement by RVoG model inversion, is presented in Figure 4.4 together with annotated HUTSCAT measurement tracks. The forest height estimates from E-SAR measurement and model inversion were converted to the HUTSCAT range profile coordinates to compare the estimates directly on the HUTSCAT measured backscattering profiles. Part of the typical HUTSCAT X-band forest profile accompanied with L-band and X-band E-SAR forest height estimates are presented in Figure 4.5. The top profile shows a HUTSCAT profile with an estimated ground line (red line) and tree top measurement (yellow dots), the middle profile shows a HUTSCAT profile with inversion results for L-band (green dots) and the bottom profile shows a HUTSCAT profile with experimental X-band inversion results (red dots). On the x-axis is HUTSCAT sample number, corresponding to helicopter forward velocity (sample step on the ground is approximately 1.3 m), and the y-axis is the HUTSCAT vertical range. Lighter areas correspond to backscattering (dB) from trees and ground. The red line in all profiles corresponds to the HUTSCAT detected ground level.

The results in Figure 4.5 indicate that the estimates derived from L-band Pol-InSAR model inversion are in a good agreement with the HUTSCAT measurements. Single measurements are somewhat noisy, but the general trend follows the tree top level quite closely. It seems that some of the Pol-InSAR-derived tree heights are slightly underestimated. For very sparse (open-canopy) forest, seen on the right-hand side of the image, the Pol-InSAR estimates at L-band underestimate the tree heights.

The experimental X-band derived canopy height estimates are shown in the bottom profile. The inversion is underdetermined and possible only under rather strong assumptions. However, as seen in Figure 4.5 the obtained X-band estimates perform well. Despite some overestimation and noise effects, the X-band estimates seem to follow both the actual tree crown structure and detect the gaps between the trees even better than at L-band. When using 60 sample average blocks along the HUTSCAT track ($\approx$75 m), the correlation between HUTSCAT height estimates and E-SAR L-band heights is $R = 0.77$, the corresponding value for X-band is $R = 0.75$. The correlation between X-band height and stand mean height from inventory is $R = 0.68$ and for L-band $R = 0.64$. The low correlation

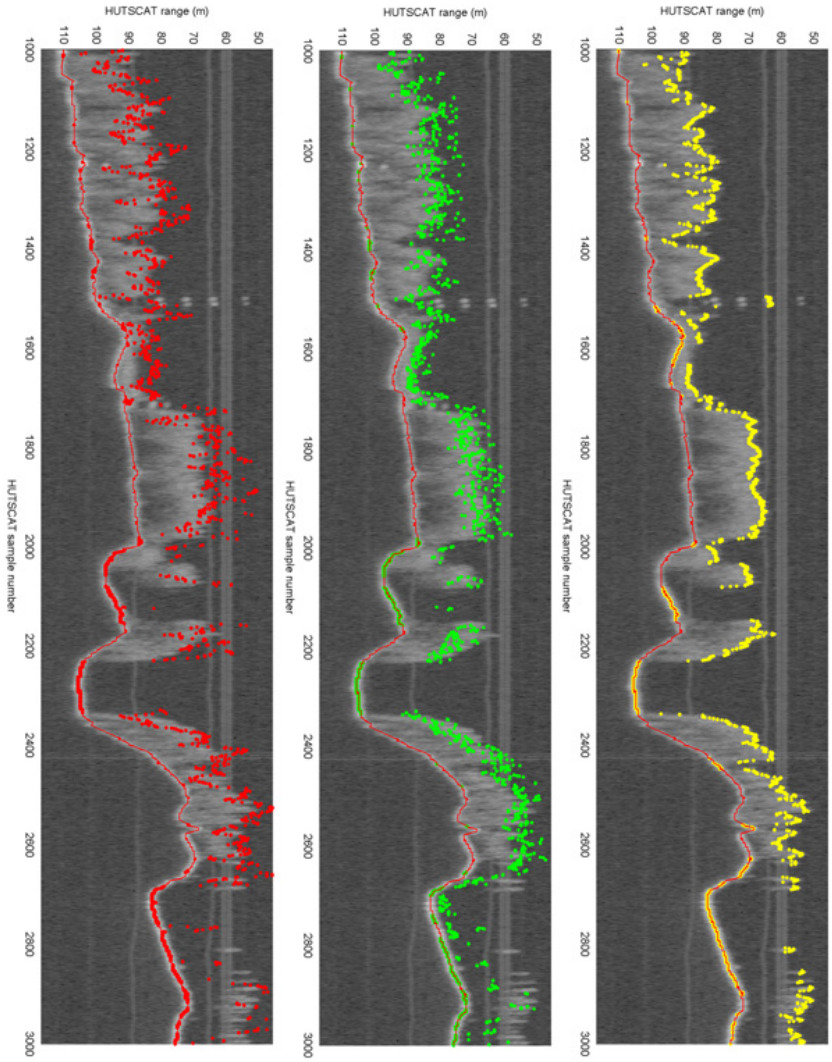

Figure 4.5. E-SAR measured tree height compared to HUTSCAT profiles. The top image shows the HUTSCAT profile with an estimated ground line and tree top measurement, the middle profile shows the same profile with L-band derived tree height and the bottom profile shows X-band tree height inversion results on top of the HUTSCAT profile. The x-axis is HUTSCAT sample number and the y-axis is HUTSCAT vertical range.

between forest inventory stand mean height and SAR derived height is explained partly by the fact that the stand mean height measurement does not describe well the canopy height in a heterogeneous forest. More suitable dominant height information was not available. When interpreting the results, one should take into account that SAR is a side looking instrument and the imaging geometry can introduce errors at forest edges and cause layover effects where tree hight is heterogeneous. However, for the studied stand sizes and the used SAR image resolution, the effect should be small; the assumption is also supported by the obtained correlations.

4.4 X- and L-band phase center location in boreal forest

Encouraged by the good results achieved for forest height retrieval with the RVoG model described in the last section, the work was continued with a set of more detailed studies. Instead of HUTSCAT measurements, a very accurate LIDAR measured ground and a canopy height model was acquired; these were used as a reference in the further study. The E-SAR L- and X-band scattering phase center location in a forest as well as forest attenuation parameters were studied. The validity of the used RVoG model framework was analyzed in detail. As a result, a RVoG model inversion algorithm for single polarization X-band interferometric data with the ancillary ground model was proposed and demonstrated. The work is reported in detail in Publication III.

4.4.1 LIDAR measurement transformation to SAR image coordinates

In order to analyze the LIDAR material together with the SAR measurements, the LIDAR measured terrain elevation model and canopy model were transformed to E-SAR slant range coordinates, which are the specific raw SAR image coordinates as shown in Figure 4.6. The missing pixels in the slant range maps were recovered by two-dimensional interpolation. In order to compare the LIDAR measurements with interferograms, a simulated ground phase was generated based on LIDAR measured ground model. The reference phase was also calculated for the canopy height model. As interferometric SAR is able to measure only relative elevation, the generated ground phase was fitted to E-SAR measured phase in open areas. The open areas were chosen by a simple coherence value threshold

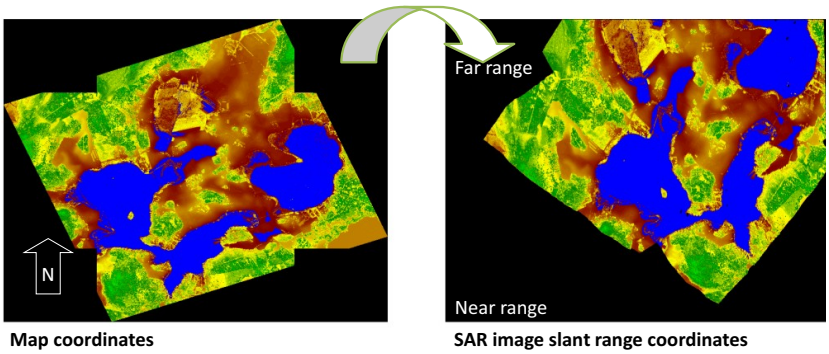

Figure 4.6. The LIDAR measured digital elevation map, provided in map coordinates(on the left) was converted to E-SAR image slant range coordinates by using E-SAR coordinate tables and interpolation.

(e.g., $\gamma < 0.97$), and appropriate parameters were obtained as a solution to the optimization problem

$$\hat{h}_f, \hat{\phi}_f = \arg\min_{h_f, \phi_f} \sum \left\| e^{i(\kappa_z(h_{DEM}+h_f)+\phi_f)} - e^{i\phi_\gamma} \right\|^2, \tag{4.11}$$

where ϕ_0 is the ground phase, κ_z is SAR vertical wavenumber, and h_f and ϕ_f are unknown constants. The latter two unknown constants were recovered by fitting the DEM-generated ground phase ϕ_0 with the SAR-measured ground phase ϕ_γ in open areas, where the SAR measurement and LIDAR reflection should come from the same height.

4.4.2 X- and L-band phase center location in the forest layer

Figure 4.7 presents the E-SAR measured interferometric phase together with the LIDAR measured reference along a selected transect line. The top profile in Figure 4.7 shows the X-band VV polarization coherence phase together with LIDAR-based ground phase estimate and a tree canopy top phase estimate. It should be pointed out that whereas LIDAR measures mostly in the nadir direction, SAR measurement is performed at the oblique incidence angle. This causes a small mismatch between the elevation data in areas where elevation changes quickly, e.g. forest edges and areas with a rapidly changing height profile. The range index on the x-axis refers to the E-SAR range coordinate for the slant range image and therefore the SAR measurement has been created from the left in relation to the presented profiles. However, in the following analysis this effect has been not taken into account because the phenomenon is mostly shadowed by co-registration error and averaging window caused artifacts.

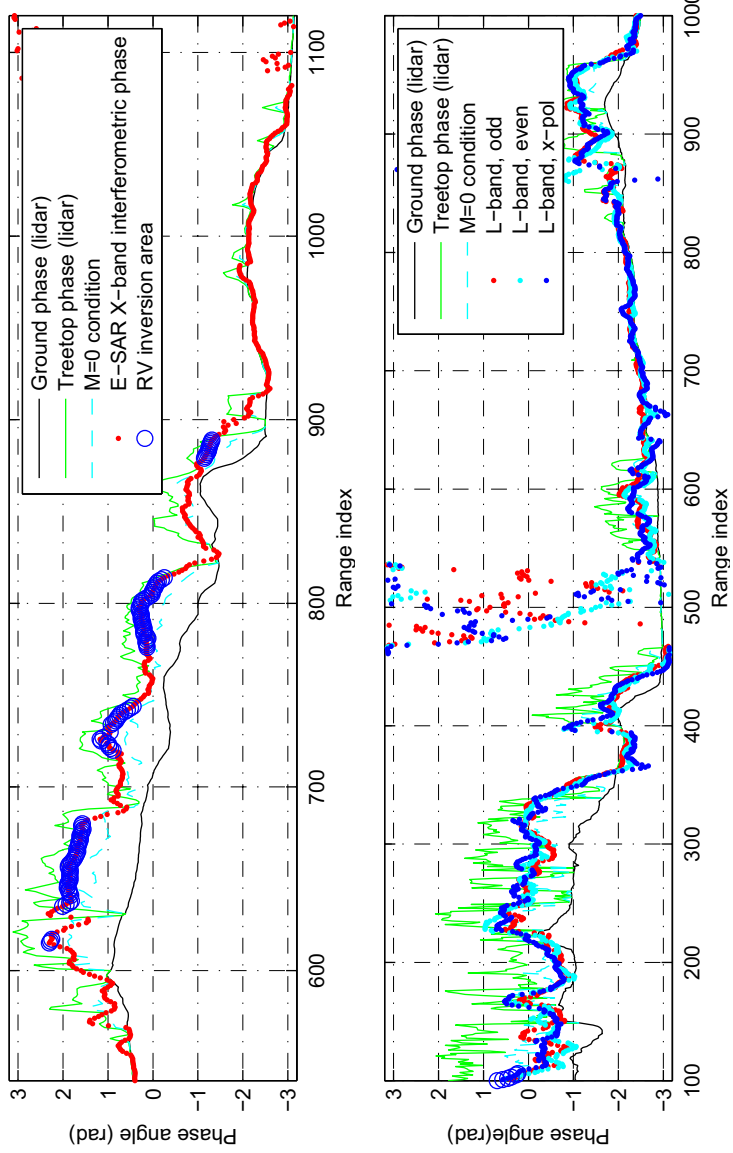

Figure 4.7. X- and L-band SAR image interferometric phase center in relation to an accurate ground and forest model. The top image shows X-band VV polarization coherence phase along the range shown with the LIDAR-based ground and canopy top phase estimate. The bottom image shows L-band coherence phase for different polarizations (Odd=HH+VV, Even=HH-VV, X-pol=HV) along the range with the LIDAR-based ground and canopy top phase estimates. ©2012 IEEE.

The result shows that the ground phase fit is good and follows the X-band coherence phase well for open areas. Additionally, the X-band coherence phase is located typically in the upper quarter of the forest canopy. The X-band coherence phase follows the forest treetop line rather well, although more smoothly due to coherence window averaging. The bottom profile in Figure 4.7 shows a similar profile for L-band. The phase center is shown for different polarization combinations. The ground phase fit is not as good as for X-band data; this is probably due to the repeat-pass configuration of the L-band measurement and some penetration into soil. The scattering center height differences between polarizations are surprisingly small and indicate a domination of the volume scattering component. The relationship between the scattering center height and the LIDAR measured tree height is presented in more detail in two-dimensional histograms as seen in Figure 4.8.

Figure 4.8 (a) shows the X-band phase center height plotted against LIDAR measured tree height. The correlation is high; however, the phase center is located approximately 25% below the the tree top, denoted with a solid black line. For canopies lower than 10 m in height the scattering center loses its good correlation with the LIDAR-based tree height, being often less than half of the measured tree height. This indicates that for forest stands with a height below 10 m, X-band coherence typically contains already a significant ground contribution for the studied forests.

The Figure 4.8 (b) shows the same for L-band HV polarization, for which an optimum correlation was obtained. Variability of the scattering center height inside the canopy at L-band is clearly larger than at X-band, indicating a significant influence from the ground contribution. The phase center height is typically around 50 % of the tree canopy height level or below that. According to the interpretation based on the RVoG model, this cannot occur without a ground contribution in SAR backscattering.

4.5 Forest height estimation from L- and X-band E-SAR images using RVoG model inversion and an accurate ground model

As indicated in Figure 4.8, the interferometric scattering phase distance from the ground correlates already well with the tree canopy height and can be used to estimate tree height with a simple model when the ground phase is known from other sources. However, SAR pulse penetrates in differing forest types to different depths and a simple phase model would

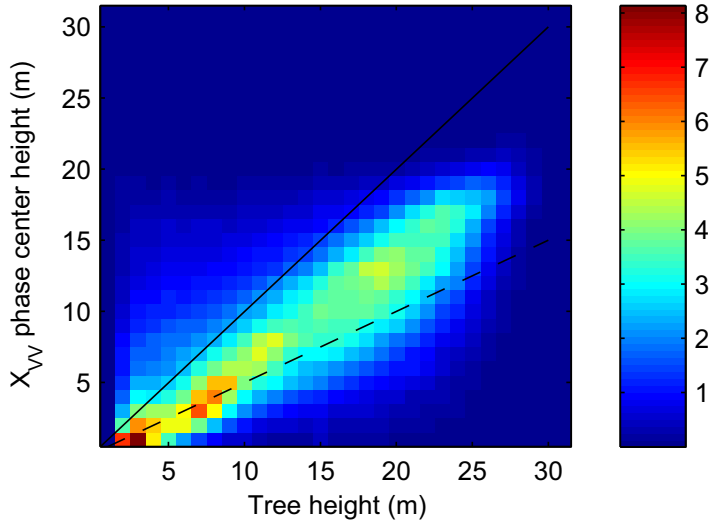

(a) X-band.

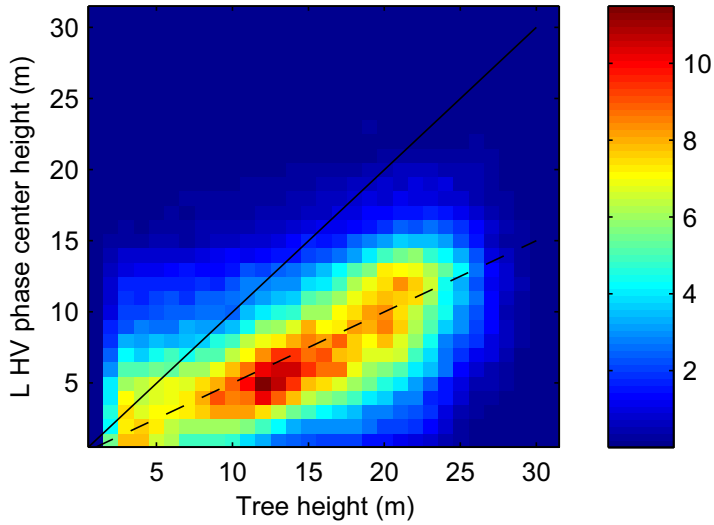

(b) L-band.

Figure 4.8. 2D histograms indicating the relationship between the interferometric phase center height [m] and the LIDAR measured tree height [m] for the test site. The image (a) shows the X-band VV polarization and the image (b) the L-band HV polarization. The solid and dashed lines correspond to treetop and 50% of the tree height locations measured by LIDAR, respectively. One unit on the color bar corresponds to 1000 samples.

be unable to compensate for these effects. The variability in penetration depth is more prominent for longer wavelengths as seen in Figure 4.8 where X- and L-band phase height is compared with LIDAR measurements in a scatterplot. In order to improve forest height estimation, coherence magnitude should be used as well, as it also contains information about the forest height, as shown in (4.7). The RVoG model is a good candidate for inversion since it relates both coherence phase and amplitude information with forest parameters. Although the RVoG model is highly simplified, it still contains too many unknowns for a full inversion using just one single polarization interferometric SAR measurement.

4.5.1 Inversion procedure

The RVoG model has four unknown parameters and single polarization interferometric coherence provides only two independent observables. One way to reduce the number of unknowns is to find areas where the ground contribution is very small or absent altogether. In this case the parameter M from (4.5) can be eliminated. Those areas (4.6) can be inverted when ground phase is accounted for and tree height can be retrieved. It is shown in Publication III that, when using the RVoG model and *a priori* knowledge about forest height, it is possible to find areas where the ground contribution should be very small. The proposed RVoG model inversion procedure with known ground phase is depicted in Figure 4.9. For the inversion, data is divided into two classes; one where ground is visible and another where ground reflection is probably missing or is very small. For areas without ground contribution (4.6) is inverted and for other areas the inversion is made with a fixed ground contribution and known ground phase for (4.5). As a side product, the inversion also produces estimates for the extinction coefficient for areas where no ground contribution assumption is applied. The inversion procedure is explained in detail in Publication III.

4.5.2 Results of forest height estimation

Figure 4.10 shows the results of the RVoG model inversion with supplemental ground phase for X-band VV polarization and for L-band HV polarization in comparison with the LIDAR measured tree canopy height. The blue dots represent tree height estimates from the volume decorrelation model (4.6) inversion for X-band while cyan dots show pixels where

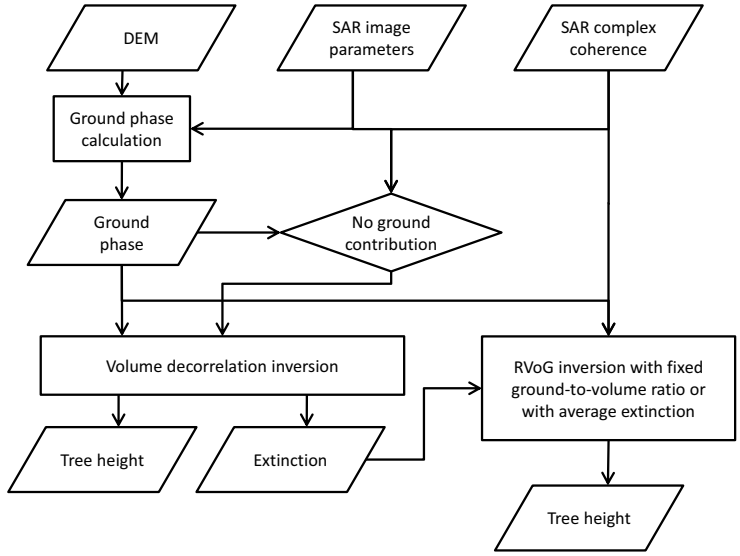

Figure 4.9. Flowchart of RVoG model inversion for single polarization interferometric data with the help of an external digital elevation map. ©2012 IEEE.

the RVoG model (4.5) inversion with a small ground contribution was used. The black dots represent tree height estimates based on L-band and volume decorrelation inversion (the case of (4.5) where $M << 1$ and ϕ_0 is known) and the red dots correspond to simplified inversion from interferometric height under a zero ground contribution and a zero forest extinction assumption. The range index on the x-axis refers to the E-SAR range coordinate for the slant range image. The inversion results follow very well the LIDAR measured tree line and it can be concluded that the proposed inversion works well. This indicates that the phase center height, especially for higher frequencies, follows the canopy top line closely. The small penetration can be very accurately compensated for with a random volume model (4.5), as also shown also in Figure 4.11, where a pixel by pixel comparison between LIDAR and SAR tree height estimates is shown. When considering that no averaging other than a coherence calculation is used in the comparison, the presented result is very good. Finally, Figure 4.12 shows the LIDAR measured forest height map compared with the X-band SAR measured forest height map. As can be seen, both forest height maps are highly detailed and very similar to one another. This result underlines the good performance of the proposed RVoG model inversion scheme.

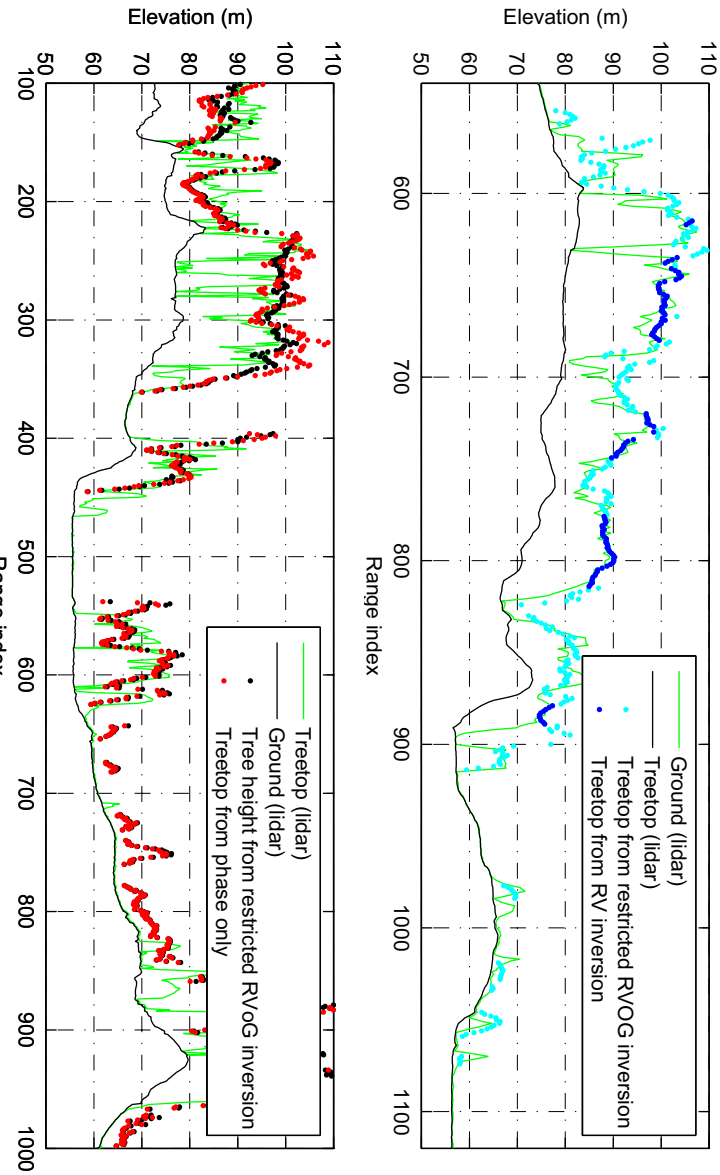

Figure 4.10. Tree height from the proposed RVoG inversion compared with LIDAR measurement along the transect line. In the top profile the results for X-band, are presented. The blue dots represent tree height estimates based on volume decorrelation while the cyan dots indicate the RVoG model inversion results with a fixed ground contribution. The bottom image shows the results for L-band. The black dots represent tree height estimates based only on volume decorrelation inversion and the red dots present the results from the simplified RVoG inversion under a zero ground contribution and a zero forest extinction assumption.

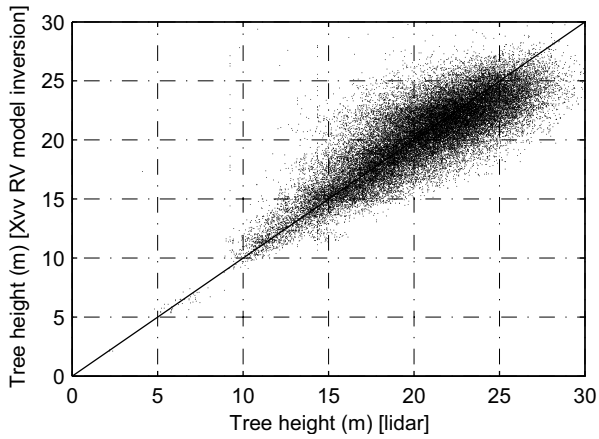

(a) X-band.

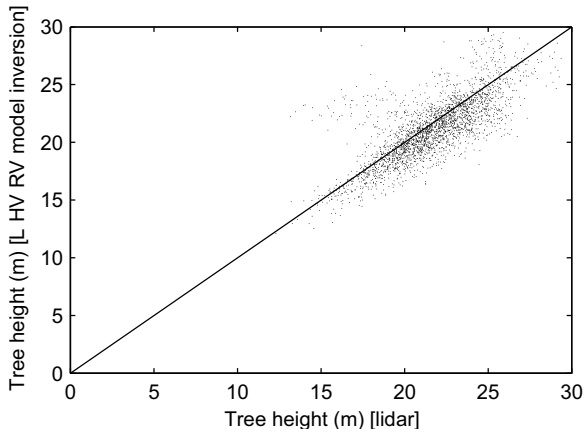

(b) L-band.

Figure 4.11. Tree height estimated from X- and L-band single channel interferometry calculated with the RVoG model and LIDAR measured ground model, when compared with LIDAR measured tree height, for areas where ground contribution is very small. ©2012 IEEE.

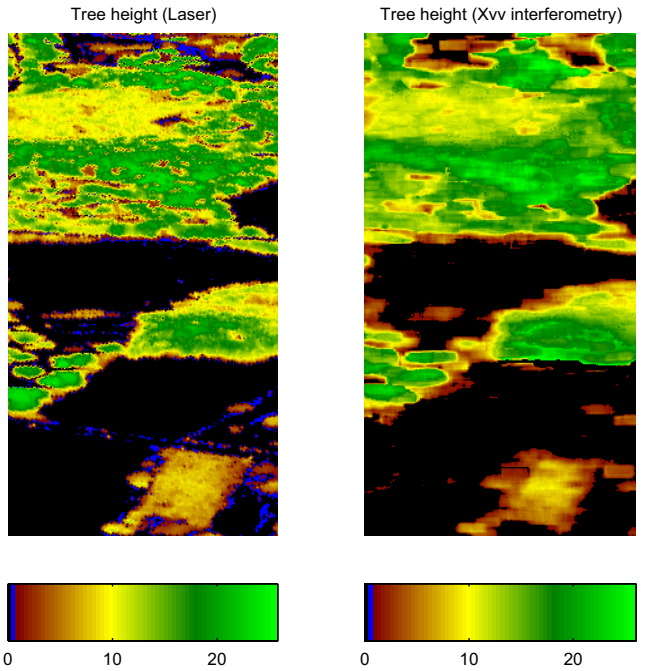

Figure 4.12. Left: tree height map (m) estimated from LIDAR measurement. Right: tree height (m) estimated from X-band interferometry. ©2012 IEEE.

4.6 Conclusions of the chapter

The Presented results from the FINSAR campaign analysis show that SAR interferometry can yield valuable information regarding boreal forests. Forest height estimation by means of L-band interferometric polarimetry and full inversion of the Random Volume over Ground model performed well in a test area forest. It was determined that the Pol-InSAR-derived height agrees with independent tree height measurements made with the HUTSCAT profiling scatterometer and LIDAR scanning. For the first time it was demonstrated that, despite the short wavelength, X-band interferometric measurements can be used for forest height retrieval at least for boreal regions. A more detailed study demonstrated that the L-band interferometric scattering center is close to half of the forest height while the X-band interferometric scattering center is usually inside the top quarter of the forest height. The detailed study also revealed that the X-band extinction coefficient in the mapped forests appeared to be somewhat lower than expected.

It was demonstrated that an accurate topographic map improves RVoG model inversion and allows retrieval of forest height even from single

channel interferometric X-band measurement. This can lead to important applications concerning the TanDEM-X mission's data utilization. Usually ground elevation changes very slowly in time and several countries have already good quality topographic information available. For example Finland in its entirety has recently been mapped using highly accurate LIDAR scanning. By combining existing topographic information with frequent SAR measurements, continually updated biomass maps for large areas should be possible. However, before the method can be utilized, the seasonal dynamics of the scattering center should be determined and the method's overall accuracy should be assessed. Also, the canopy height relation to the biomass needs further study as the relation is species specific and depends on many variables. As SAR backscattering depends on forest structure related parameters, a more direct link to biomass could be established even without accurate tree height measurement. The SAR based methods cannot compete in tree height measurement with LIDAR measurement accuracy, but high resolution satellite SAR interferometry shows promising prospects for global biomass mapping even with the currently existing spaceborne systems.

5. Modeling radar scattering from single trees

With the wider use of fully polarimetric and interferometric measurements, where an accurate phase needs to be measured, the demand for coherent scattering models has grown. As was demonstrated in Chapter 4, a forest scattering model can provide valuable information about the behavior of polarimetric and interferometric parameters and help to estimate forest properties, such as tree height, from SAR images. The RVoG model, which was used in Chapter 4 is, however, a very simple model and it is not suitable for studying polarization effects caused by tree geometry, influence of small parts and orientation related and small scale effects. For detailed studies, more complex models which describe trees more accurately are being actively developed and examined. For example a coherent backscattering model for a forest in [32] was used to investigate polarimetric and interferometric responses [33, 59]. Also for a mangrove forest a coherent scattering model was developed in [67]. In this chapter the scattering models for coniferous trees is taken to the next level by calculating scattering for a pine tree with needle level accuracy. It is shown, how a detailed tree model can be used to study large scale scattering effects and how the results can be linked to SAR measurements.

This chapter is organized as follows: in Section 5.1 a detailed scattering model, which is used in the work, is described. In Section 5.2 the model is used to calculate backscattering from an idealized pine tree and a method is proposed to link tree model calculation by statistical means to the SAR measurement of a larger forest patch. The work was published mainly in Publication IV and also in [55, 44, 56]. In Section 5.3 the model is used to calculate the scattering properties of an idealized pine tree, complete with needles, and is compared with a rigorous volume integral scattering model. This work is published in Publication V. Finally, conclusions of the chapter are presented in Section 5.4.

5.1 Scattering model based on Infinite Cylinder Approximation (ICA)

A relatively straightforward field model [75, 60] is used in this work to calculate radar scattering from trees. The model is an electric field computing model, able to calculate the far field from an arbitrary structure made of homogeneous dielectric cylinders illuminated by a plane wave. The calculation is based on the truncated Infinite length Cylinder Approximation (ICA) [61]. The tree or trees are built from cylinders, representing trunk sections, branches, and even needles in the case of coniferous trees. The model accounts for all material involved in the scattering, calculates direct reflections from cylinders and reflections from the ground. The accuracy of the model is restricted mainly by the infinite cylinder approximation, ground model, and the fact that higher order reflections are neglected. The model was developed by a larger consortium during the MODAFOR (New Modeling and Data Analysis Methods for Satellite Based Forest Inventory) project, in which the author also participated.

5.1.1 Scattering amplitude and scattering matrix

A short description of the employed ICA model is given in the following subsection. The definition is based on [60].

The scattered far field $\boldsymbol{E}_s(\boldsymbol{r})$ of a three dimensional scatterer W, when illuminated with incident plane wave $\boldsymbol{E}_i(\boldsymbol{r})$, can be written as

$$\begin{bmatrix} E_{V_s} \\ E_{H_s} \end{bmatrix} = F(\hat{\boldsymbol{k}}_s, \hat{\boldsymbol{k}}_i) \begin{bmatrix} E_{V_i} \\ E_{H_i} \end{bmatrix}, \tag{5.1}$$

where scattering matrix F can be written as

$$F(\hat{\boldsymbol{k}}_s, \hat{\boldsymbol{k}}_i) = \begin{bmatrix} f_{VV} & f_{VH} \\ f_{HV} & f_{HH} \end{bmatrix}, \tag{5.2}$$

and where the scattering matrix components $f_{\beta\alpha} = f_{\hat{\boldsymbol{\beta}},\hat{\boldsymbol{\alpha}}}(\hat{\boldsymbol{k}}_s, \hat{\boldsymbol{k}}_i)$ are given with respect to incident and scattered polarization orientations $\hat{\boldsymbol{\beta}}, \hat{\boldsymbol{\alpha}}$ and the incident and the scattered directions $\hat{\boldsymbol{k}}_s, \hat{\boldsymbol{k}}_i$. Here the horizontal H and vertical V polarization basis is used. Note that the scattering matrix F (5.1) is written here according to the Forward Scattering Alignment convention (used in physics) and the scattering matrix S (3.1) was on the other hand written in Chapter 3 according to the Back Scattering Alignment (used in engineering) [36].

By translation and rotation of the scattering matrix F the scatterer W can be moved in the space. It can be shown that the scattering matrix of the scatterer W, translated by a vector $\boldsymbol{p}$, transforms to scatterer $W_{\boldsymbol{p}}$ scattering matrix $F_{\boldsymbol{p}}$ as

$$F_{\boldsymbol{p}}(\hat{\boldsymbol{k}}_s, \hat{\boldsymbol{k}}_i) = e^{-ik_0 \boldsymbol{p}\cdot(\hat{\boldsymbol{k}}_s - \hat{\boldsymbol{k}}_i)} F. \tag{5.3}$$

In order to change the orientation of the scatterer, the unitary rotation matrix U can be used. The scattering matrix F_U of the rotated scatterer W_U can be written as the product of five matrices,

$$\begin{aligned} F_U(\hat{\boldsymbol{k}}_s, \hat{\boldsymbol{k}}_i) &= \begin{bmatrix} \hat{\boldsymbol{v}}_{\boldsymbol{s}}^{\boldsymbol{T}} \\ \hat{\boldsymbol{h}}_{\boldsymbol{s}}^{\boldsymbol{T}} \end{bmatrix} \begin{bmatrix} \hat{\boldsymbol{v}}_s', & \hat{\boldsymbol{h}}_s' \end{bmatrix} A, \\ A = F(U^T \hat{\boldsymbol{k}}_s, U^T \hat{\boldsymbol{k}}_i) &\begin{bmatrix} \hat{\boldsymbol{v}}_i'^T \\ \hat{\boldsymbol{h}}_i'^T \end{bmatrix} \begin{bmatrix} \hat{\boldsymbol{v}}_i, & \hat{\boldsymbol{h}}_i \end{bmatrix}, \end{aligned} \tag{5.4}$$

where $\hat{\boldsymbol{h}}_j' = (U\hat{\boldsymbol{z}}) \times \hat{\boldsymbol{k}}_{\boldsymbol{j}} / \left| (U\hat{\boldsymbol{z}}) \times \hat{\boldsymbol{k}}_{\boldsymbol{j}} \right|$, $\hat{\boldsymbol{v}}_j' = \hat{\boldsymbol{h}}_j' \times \hat{\boldsymbol{k}}_{\boldsymbol{j}}$, $j = i, s$, are the rotation and translation matrices [60]. By translating and rotating the single cylinder scattering matrix, a cylinder structure can be created when the scattering matrix of the cylinder is known.

5.1.2 Scattering from a finite cylinder

The scattering matrix of a finite cylinder can be computed in a fast manner by using the truncated infinite length cylinder approximation [61]. The idea is to calculate analytically scattering from an infinite cylinder

$$\boldsymbol{E}_\infty(\hat{\boldsymbol{k}}_s) = \frac{k_0^2}{4\pi} \frac{(\varepsilon - \varepsilon_0)}{\varepsilon_0} (I - \hat{\boldsymbol{k}}_s \hat{\boldsymbol{k}}_s^T) \int_V e^{-ik_0 \hat{\boldsymbol{k}}_s \cdot \boldsymbol{r}} \boldsymbol{E}_{\mathrm{vol}}(\boldsymbol{r}) dV \tag{5.5}$$

and then approximate the volume current by that of the corresponding infinite cylinder restricted to the volume of the finite cylinder. This means that $\boldsymbol{E}_{\mathrm{vol}}(\boldsymbol{r})$ in (5.5) is approximated by the total field of the infinite cylinder, whose electric field can be expressed in an analytic form by using cylindrical wave functions and cylindrical coordinates (r, ϕ, z),

$$\boldsymbol{E}_{\mathrm{vol}}(\boldsymbol{r}) \approx \sum_{n=-\infty}^{\infty} e^{-in(\phi_i - \pi/2)} \boldsymbol{E}_n(r, \phi) e^{in\phi} e^{ik_z z}. \tag{5.6}$$

The components of the scattering matrix F can be then written in the form of

$$\begin{aligned} f_{VV} &= -2\pi D \left(\frac{\sin\theta_s}{k_z} Z_0 + \frac{\cos\theta_s}{k_{1r}} Z_1 \right) a_{0,v} + \\ &\quad D \sum_{n=1}^{\infty} (iA_{n,v} + C_{n,v}) \cos(n(\phi_s - \phi_i)), \\ f_{VH} &= D \sum_{n=1}^{\infty} (-A_{n,h} + iC_{n,h}) \sin(n(\phi_s - \phi_i)), \\ f_{HV} &= D \sum_{n=1}^{\infty} iB_{n,v} \sin(n(\phi_s - \phi_i)), \\ f_{HH} &= D \frac{-2\pi}{k_{1r}} Z_1 b_{0,h} + D \sum_{n=1}^{\infty} B_{n,h} \cos(n(\phi_s - \phi_i)), \end{aligned} \tag{5.7}$$

where $D, a_{n,t}, b_{n,t}, A_{n,t}, B_{n,t}, C_{n,t}$, for $t = v, h$, and Z_n are given in [60].

5.1.3 Coherent scattering from a collection of cylinders

A tree is modeled as a collection of finite homogeneous dielectric cylinders that represent the trunk, the branches and the needles. For every cylinder the scattering matrix is calculated according to the ICA approximation and moved to the correct position by translation and rotation. The scattering matrix F of an entire tree is obtained by adding (coherently) the scattering matrices of its cylindrical parts F_n as

$$F(\hat{\boldsymbol{k}}_s, \hat{\boldsymbol{k}}_i) = \sum_{n=1}^{N} F_n(\hat{\boldsymbol{k}}_s, \hat{\boldsymbol{k}}_i), \tag{5.8}$$

where N is the number of cylinders in the model tree. Computing the scattering matrix of a tree in such a way takes into account the direct scattering from all individual cylinders, but ignores all multiple scattering between the cylinders. The scattering interaction between a tree and the horizontal ground is taken into account by adding the ground bounce terms for three scattering paths: ground-scatterer, scatterer-ground, and ground-scatterer-ground. The ground is modeled as a layered half-space instead of using a more realistic random surface model like in [28]. The ground bounce terms

$$\begin{aligned} f^{\text{total}}_{\beta,\alpha}(\hat{\boldsymbol{k}}_s, \hat{\boldsymbol{k}}_i) &= f_{\beta,\alpha}(\hat{\boldsymbol{k}}_s, \hat{\boldsymbol{k}}_i) + R_\alpha(\hat{\boldsymbol{k}}_i) f_{\beta,\alpha}(\hat{\boldsymbol{k}}_s, \hat{\boldsymbol{k}}^b_i) + \\ R_\beta(-\hat{\boldsymbol{k}}_s) f_{\beta,\alpha}(\hat{\boldsymbol{k}}^b_s, \hat{\boldsymbol{k}}_i) &+ R_\alpha(\hat{\boldsymbol{k}}_i) R_\beta(-\hat{\boldsymbol{k}}_s) f_{\beta,\alpha}(\hat{\boldsymbol{k}}^b_s, \hat{\boldsymbol{k}}^b_i), \end{aligned} \tag{5.9}$$

are added to the direct scattering matrix (5.8) coherently [60]. In (5.9) α is the incident vertical or horizontal polarization and β is the scattered polarization respectively.

This simple model contains the key interactions for polarimetric scattering from a tree in an electromagnetically exact way, namely the direct coherent scattering from the tree and the coherent ground reflection. Therefore, the model allows the examination of the coherent effects in scattering from the tree as well as study the importance of incoherent and higher order effects. For a sparse constellation of relatively thin cylinders the model accuracy should be very good, of course assuming that the modeled structure is well described by a collection of homogeneous dielectric cylinders over a smooth surface. The model is fully coherent, fully polarimetric and bistatic, allowing one to choose the illumination and scattering directions freely. The output of the model is the scattering matrix F defined for incident and scattered plane wave electric field E horizontal H and vertical V components $f_{HH}, f_{HV}, f_{VH}, f_{VV}$ [60].

5.2 Scattering statistics of a pine tree calculated with the ICA model

In this section the ICA model is used to calculate bistatic and monostatic scattering patterns of a pine tree at L-band. It is demonstrated that scattering from a single direction is not sufficient to describe the tree and a method to calculate scattering statistics, comparable with methods used in SAR polarimetry, is proposed. The work is reported in full detail in Publication IV.

5.2.1 Cylinder model of a pine tree

For this study a model of a 45-year old pine tree of height 15 m consisting of 8531 cylinders is used, see Figure 5.1. The tree cylinder model is generated by the LIGNUM tree growth model [43, 42] which is based on extensive studies of tree growth in Finland. It uses a Lindenmayer-systems-like [57] fractal approach to simulate tree growth and structure, and it is able to generate photo-realistic virtual trees. The tree in this simulation does not include needles.

Often in polarimetric scattering models for vegetation and forest, needles or leaves are taken into account by an additional canopy attenuation model [32, 4]. However, for the current study it was decided to leave the needles out for two reasons: a) to reduce computational load, and b) the needles have a relatively small contribution to L-band scattering where

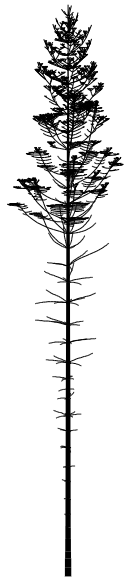

Figure 5.1. A model of a 45-year old pine tree of height 15 m, consisting of 8531 cylinders, generated by the LIGNUM tree growth model [43].

the wavelength approximately 5 times longer than a needle. Attenuation is not additionally accounted for. The complex relative permittivity for the cylinders and the soil is $\epsilon_{\text{tree}} = 15 + 5i$ and $\epsilon_{\text{soil}} = 7 + 1i$, respectively, which should describe snow covered ground in winter conditions according to [22]. Values were chosen for comparison with existing L-band SAR data.

5.2.2 Utilization of tree rotational symmetry to generate scattering statistics

Figure 5.2 presents the bistatic (incident and scattering directions are separated by a constant 3^0 difference) scattering amplitude from a pine tree as a function of tree rotation angle, calculated with the ICA model. Scattering is variable in different directions and obviously a value calculated for a single direction does not give very much information about the scattering of an entire tree. Simulations show that the scattering matrix values are also very sensitive to the position of the receiver, as can be appreciated in Figure 5.3, where spherical scattering patterns of the same tree are presented. Figure 5.3 shows the patterns for the tree (a) without the ground and (b) with the ground included. The virtual transmitter is denoted with a red box. The scattering is highly variable and ground reflections create very strong peaks.

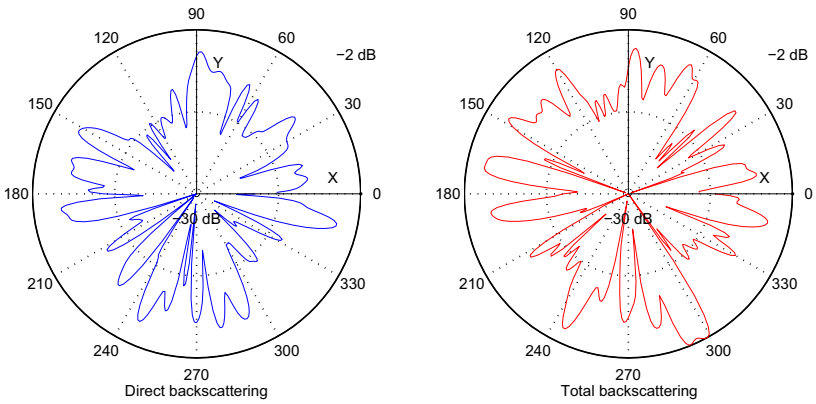

Figure 5.2. Bistatic scattering amplitude from the tree as a function of the azimuth angle of the scattering direction at L-band, HH polarization. The virtual source and the receiver are separated by 3^0. The polar angle is $\theta = 50^0$. The left side panel shows direct scattering while the right side panel indicates total scattering including ground. The scale for scattering level is from -30 dB in the center to 34 dB on the outer ring.

High variation applies to both bistatic and monostatic simulations. Instead of a single simulated value, a larger ensemble of values should be used to describe the scatterer. It is proposed in Publication IV that scattering statistics could be generated by rotating the tree model with respect to the vertical axis and the generated values should be summarized by using a covariance matrix formalism.

In SAR image analysis it is normally assumed that there is a large amount of scatterers in a resolution cell. This assumption leads to the conclusion that the observables are statistically distributed according to the multivariate complex Gaussian distribution [39]. The observable, in this case, is the scattering vector, formed from scattering matrix elements as presented in (3.4). The multivariate Gaussian distribution should be described completely by the covariance matrix (3.3). Consequently, the covariance matrix estimate is a good and compact description of a distributed homogeneous scatterer. The averaged covariance matrix preserves information regarding average power and the average phase differences between the scattering matrix elements but ignores the absolute phase information. However, the presence of texture requires a more general K-distribution [39].

It was found that the behavior of L-band polarimetric SAR measurements for coniferous forests mostly follows the Gaussian distribution [58], hence the model derived values for pine should do likewise. The validity

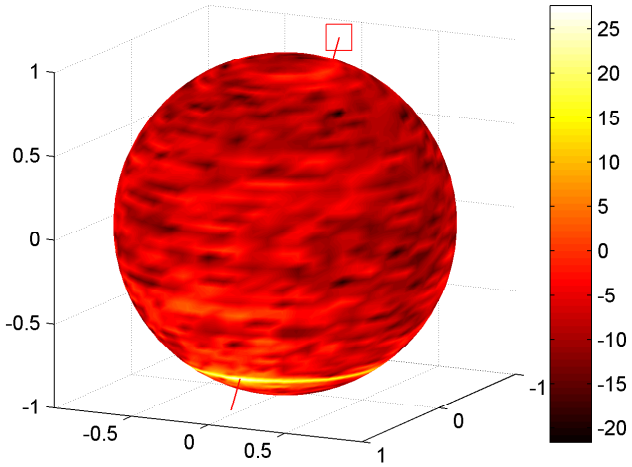

(a) Scattering from the pine tree without ground contribution.

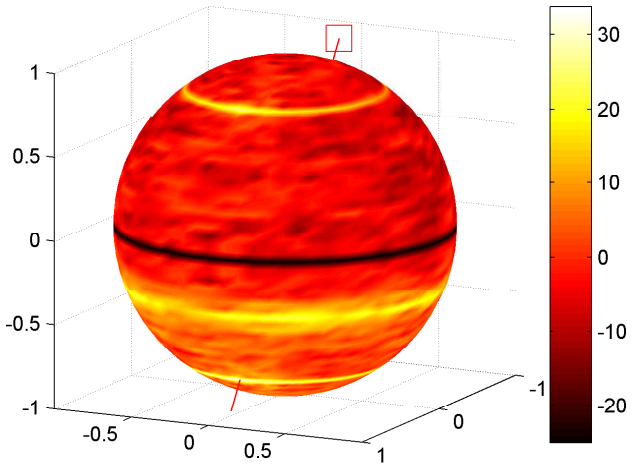

(b) Scattering from the pine tree with ground contribution.

Figure 5.3. Spherical pattern of scattered power from the pine tree model when illuminated by an L-band plane wave. The virtual plane wave source which is located at an infinite distance in the direction $\theta = 36^0$ and $\phi = 180^0$, marked with a red box in the figure. Results are presented: (a) without ground reflections and (b) with ground reflections included. Scale is in dB. ©2008 IEEE.

of this approach can be tested by checking the agreement of collected observable histograms with a theoretical distribution. The test can be made by using marginal distributions, derived for one dimensional variables. The samples used to form the statistical distribution from the ICA model calculation are collected by rotating the tree model around the vertical axis randomly and simulating the scattering matrices with the same incidence angle for the same tree repeatedly. From the calculated scattering matrix (5.1) elements a measurement vector can be formed as

$$\vec{k} = [f_{HH}, f_{HV}, f_{VH}, f_{VV}]^T . \tag{5.10}$$

If the ensemble of measurements follows a multivariate complex Gaussian distribution, its probability density function should be [39]

$$P(\vec{k}) = \frac{1}{\pi^N \det C} \exp(-\vec{k}^\dagger C^{-1} \vec{k}), \tag{5.11}$$

where C is the covariance matrix of a measurement vector $\vec{k}$ defined as in (3.1).

A total of 180 looks was generated for the monostatic setup from random directions to the previously described 45 year old pine tree. In Figure 5.4 the total scattering amplitude, amplitude ratio and phase difference histograms and the theoretical marginal distribution are compared. The goodness of fit is estimated by using a χ^2-test with 25 degrees of freedom. In two cases out of four, the error X^2 is smaller than the critical value. The deviation in the third case is explained by the fact that the ground reflection introduces a systematic texture component to the scattering.

It is concluded in Publication IV that scattering from the crown (HV polarization), where there are enough small scatterers, is described by a Gaussian distribution but for describing strong ground reflection, which introduces texture, the more general K-distribution is required. Even when the probability density function is not entirely Gaussian, the same approach can be used as it is often done in SAR image analysis, but in case of a non-Gaussian distribution, additional moments are needed for a complete description of the probability density function.

5.3 Validation of ICA model with Volume Integral Equation (VIE) model

In this section the ICA model is compared with the more accurate Volume Integral Equation (VIE) model, which takes into account all high or-

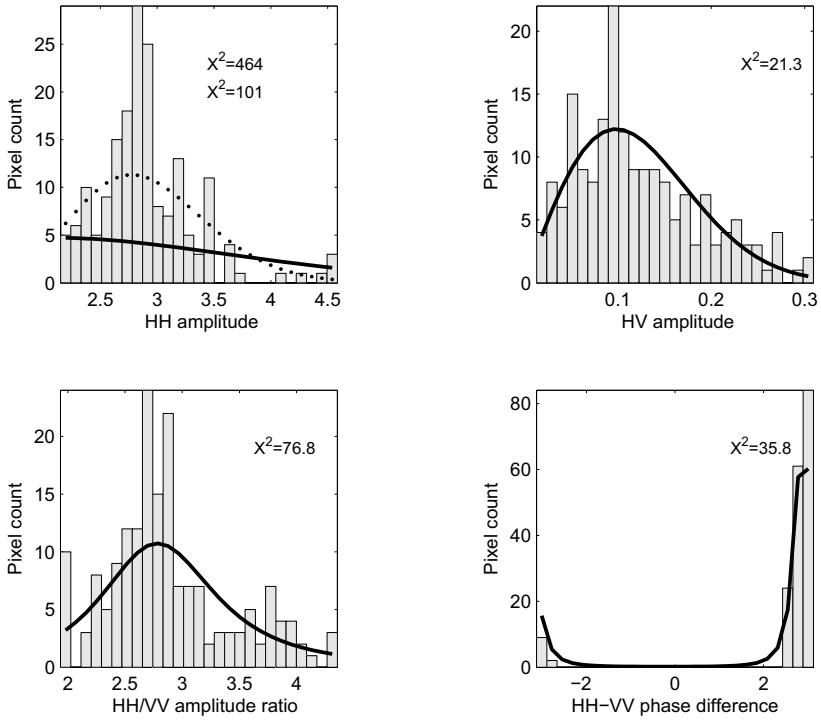

Figure 5.4. Histograms of the modeled scattering amplitude, the amplitude ratio and the phase differences for different polarizations at L-band (1.25 GHz) for the monostatic case (incidence angle 36^0). Histograms are generated by randomly rotating the tree and calculating the scattering matrix. The solid lines represent the probability density functions that correspond to the pure Gaussian assumption. The dotted line corresponds to the generalized K-distribution. The critical χ^2 value for 25 degrees of freedom and at the 95% confidence level is 37.7.

der reflections between the scatterers. Both models are used to calculate scattering in the L- and C-bands from a detailed pine tree model which also includes needles. With these calculations, both models are cross validated and the importance of multiple scattering inside the pine canopy and the contribution of the needles to scattering, is assessed. The results show that for C-band calculations the VIE model output differs from the ICA model output, indicating the importance of higher order scattering between the needles and branches. However, for L-band, the VIE model produces results similar to those from the ICA model, indicating that multiple scattering between the needles is not important. This work was reported in Publication V.

5.3.1 Compared scattering models

The two models compared in this study are: the Infinite Cylinder Approximation (ICA) model, described in Section 5.1, and an accurate Volume Integral Equation (VIE) model, accelerated with a Multi-Level Fast Multipole Algorithm (MLFMA), described in Publication V. The VIE model is able to calculate the scattering of the electromagnetic wave from a collection of cylinders with high accuracy by taking into account all interactions between the even the smallest parts of the target.

The ICA model solves the scattering problem for one cylinder at a time and adds up the scattering from all cylinders coherently. It takes into account only the direct scattering from the individual cylinders while ignoring multiple scattering between the cylinders. The VIE model, on the other hand, divides every cylinder into smaller pieces (much smaller than the wavelength) and models its scattering. The solution for the entire scattering problem is calculated as an inversion of the equation system, leading to a solution where all the interactions are taken into account. As this equation system is very large, solving it by matrix inversion would require too much computer time. Therefore, the system is solved iteratively by using generalized minimal residuals. The matrix-vector multiplication in this calculation is accelerated by the MLFMA method [3]. The MLFMA method builds a hierarchical system where the scatterer is enclosed first in a cube, which is then subdivided into eight subcubes. Each of these cubes is again subdivided into eight new cubes and this process is recursively continued. The MLFMA method builds an octree structure with multiple levels until the last cube at each branch of the octree encloses only a small number of elements. In principle, the VIE model with

MLFMA acceleration would allow one to calculate scattering from any type of object with very high accuracy. In the following, both models are applied to a detailed section of our pine tree model, complete with needles. Ground reflections are not considered in this work.

5.3.2 Pine tree model with needles

The geometry model of the studied section of a pine tree used in the calculations is illustrated in Figure 5.5. The model is again generated by the LIGNUM tree growth model which provides a cylindrical model of the trunk and branches. It also contains information about the number and average length of the needles in each branch, but not the exact location of each needle. The pine tree section used here is approximately 1.3 m long. The thicknesses of the lower end of the trunk is 2 cm while the thinnest branch is 2 mm in diameter.

The needles were added to the model according to statistical information provided by LIGNUM model. In order to avoid effects caused by regular structures, some noise was added to the the process. The needles were attached to a shoot and distributed randomly along the branch with a random azimuthal direction. An average needle elevation angle to branch was chosen to be 55^0, and it was randomly varied by 10%. The average length of the needles was 4.6 cm. The thickness of the needles was varied around 1.0 mm. The total volume of the needles is roughly two times that of the trunk and bare branches. In the case of a complete pine tree, the ratio is, of course, smaller. The trunk and bare branches consist of 118 cylinders. Including the needles the total geometry model of the tree consisted of 22 210 cylinders. The complex permitivity $\epsilon_{\mathrm{tree}} = 15 + 5i$ was assumed to be the same for all cylinders, needles included.

5.3.3 Numerical calculations and comparisons

In order to compare the two scattering models described above, a scattering matrix for the tree model was calculated by using both the ICA and VIE models. The calculations were carried out for two common radar frequencies, namely, 1.5 GHz (L-band) and 6 GHz (C-band), the corresponding wavelengths being 0.2 m and 0.05 m, respectively. An ICA-based bistatic spherical scattering pattern of the tree (Figure 5.5) at L-band is shown in Figure 5.6. The pattern is calculated by the ICA model, incident wave direction is depicted with a line, and the virtual radar is marked

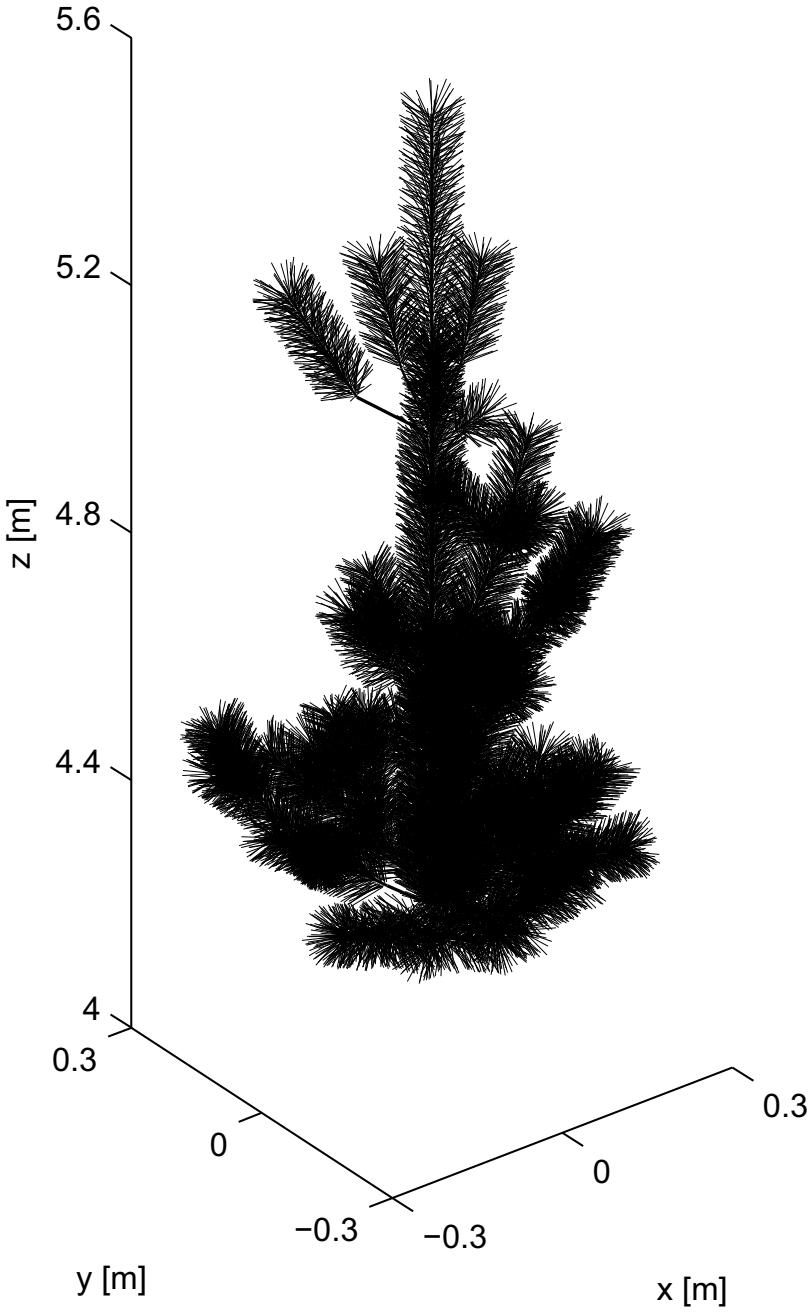

Figure 5.5. Geometry of the studied section of a pine tree. The model is generated according to the LIGNUM tree growth model [43] data and needle attachment algorithm. ©2010 IEEE.

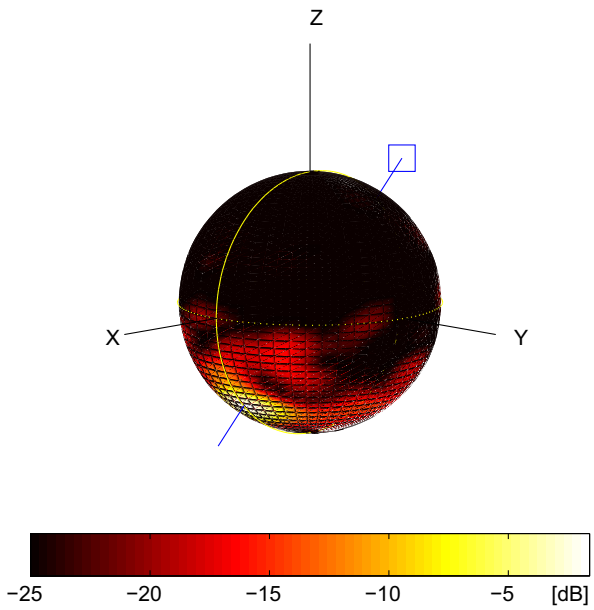

Figure 5.6. The spherical scattering pattern of the pine tree with needles, calculated with the ICA model. Color denotes the total scattered power over all polarizations in dB. ©2010 IEEE.

with a rectangle. In the image the forward scattering direction is evident as a bright area in bottom left.

For the comparison between models, the angles of the incident direction were $\theta^{\text{inc}} = 3\pi/4$, $\phi^{\text{inc}} = 0$, and the scattering matrix was calculated in two plane sections, the first one defined by $\theta^{\text{sca}} = 0, \ldots, 2\pi$, $\phi^{\text{sca}} = 0$, and the second one by $\theta^{\text{sca}} = \pi/2$, $\phi^{\text{sca}} = 0, \ldots, 2\pi$. The comparison plane section positions are presented also in Figure 5.5 using yellow lines. In order to satisfy the requirements of the approximations in VIE, the cylinders for the geometry model used by VIE had to be separated from those used in the ICA geometry model. The same set of cylinders was used for both bands, so the maximum size of a cylinder was determined by the shorter wavelength. The total number of cylinders used in the VIE calculations was 218807, which is about ten times more than used by ICA.

5.3.4 Effect of needles on scattering from a pine tree

The scattering matrix values obtained by the two models are compared in Figures 5.7 and 5.8. The values are presented along the two plane sections (azimuth and elevation) of the spherical scattering pattern, shown

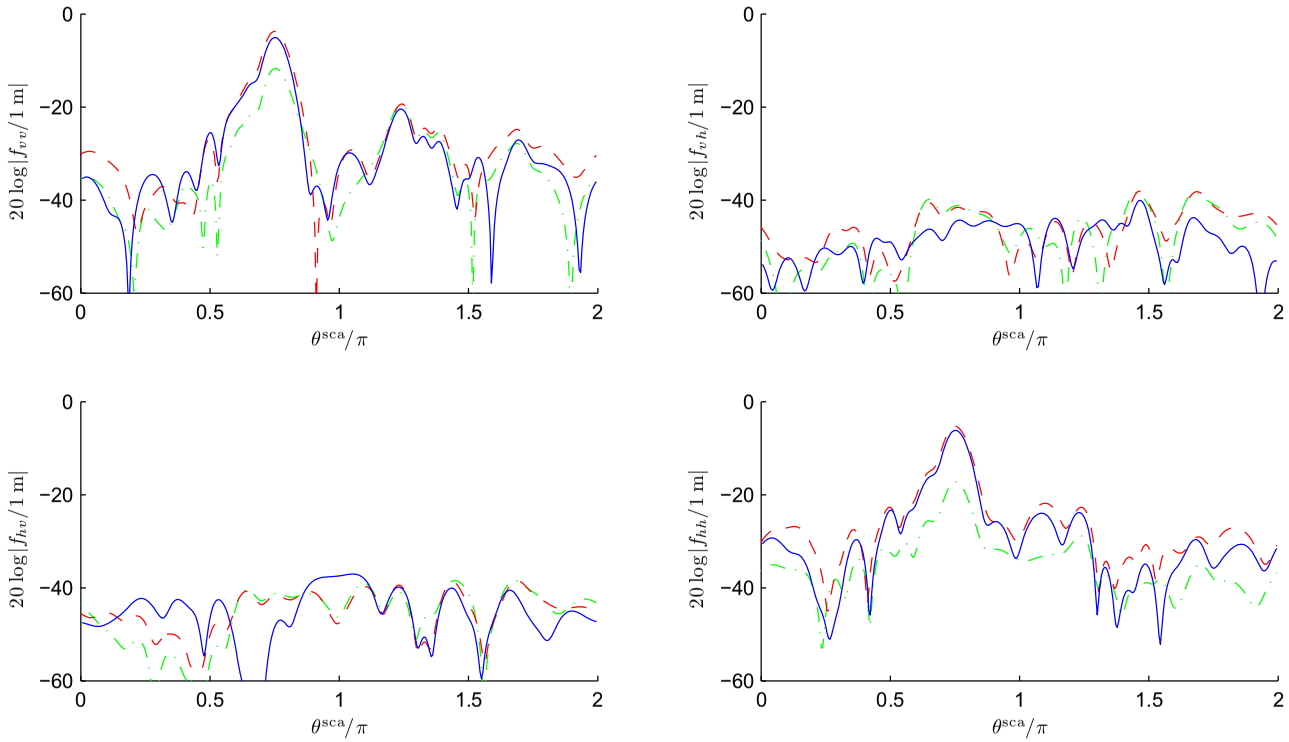

Figure 5.7. Absolute values of the scattering matrix elements at L-band in the plane $\theta^{\mathrm{sca}} = \pi/2$ calculated by using VIE (blue line) and by using ICA with (red line) and without needles (green line). ©2010 IEEE.

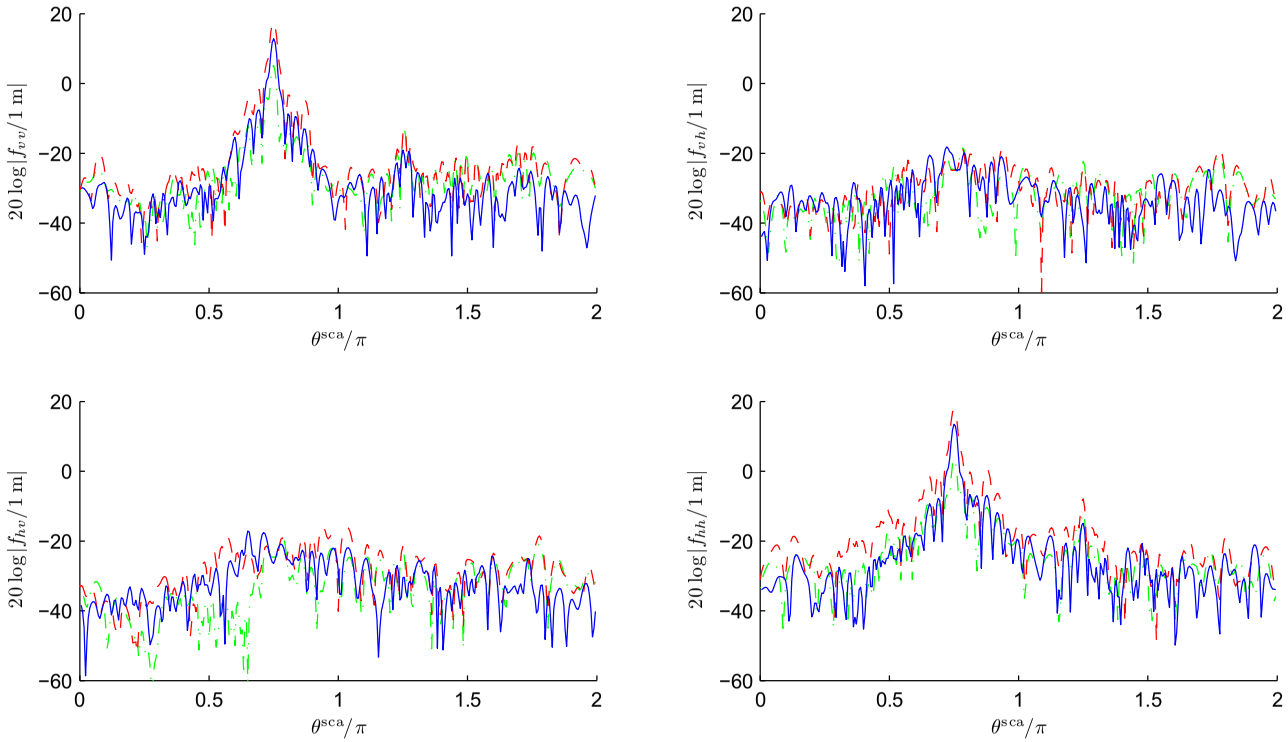

Figure 5.8. Absolute values of the scattering matrix elements at C-band in the plane $\theta^{\mathrm{sca}} = \pi/2$ calculated by using VIE (blue line) and by using ICA for the models with (red line) and without needles (green line). ©2010 IEEE.

with yellow lines in Figure 5.6. In the plots, the blue solid lines represent the results obtained by using the VIE model for the complete geometry model, including the needles. The red lines show the corresponding results obtained by using the ICA model and the green line denotes the ICA calculations for the tree without needles.

As seen in Figure 5.7 for L-band, the ICA model produces a similar scattering pattern for the tree with and without needles, the only difference being a lower amplitude, since the volume of the scatterer is smaller by the amount of the needles. Despite the fact that the simple ICA model does not take into account the interaction between cylinders, it produces results very similar to those from the elaborated VIE model. This can be true only when scattering from the needles is very weak and the interaction between small elements is not important. Also, the smooth shape of the scattering pattern suggests that scattering is dominated by tree's larger parts.

Figure 5.8 presents an analogous horizontal scattering pattern for the C-band. A similar forward scattering peak is observed at L-band, but the variation as a function of the direction is much more rapid. The ICA model produces a similar pattern without needles but with a lower amplitude. These results show that, when the radar wavelength is in the same order as the needle size or smaller, multiple scattering between the needles becomes more relevant. For longer wavelengths, however, simple models can be used successfully.

5.4 Conclusions of the chapter

In this chapter, polarimetric scattering was simulated from modeled trees using highly accurate electromagnetic models. It was shown that model calculations need to be treated statistically, as calculation for a single direction does not produce sufficient information about the target. It was shown that the coherency matrix formalism, similar to that used in SAR image analysis, can be applied also to the model calculations. The covariance matrix appears to describe the simulation well, as the underlying scattering vector distribution follows a Gaussian distribution, at least in the L-band. A new method for calculating multilook average by using a rotating tree model was proposed and successfully implemented. It can also be concluded that the covariance matrix, when averaged over the directions around a single tree can be considered representative for a larger

group of trees or a homogeneous tract of forest, as both behave statistically in a similar way.

Comparison of a simple ICA model, which does not account for higher order reflections, with an accurate VIE model revealed that at L-band needles of a coniferous tree generate no significant contribution to the scattering pattern. However, at C-band, the differences between the two models were more prominent and, therefore, with C-band simulations, needles should be accounted for. It was shown that the importance of multiple scattering inside a pine canopy and the scattering contribution of the needles becomes important when the wavelength is on the order of the needle length or shorter.

At L-band the simpler model, which does not take into account multiple scattering, produces results that are almost as good as the much more advanced model. Although the comparison was performed for only one permittivity value, the results are probably general enough to draw a conclusion. A comparison of the models shows that, at the L-band, the needles slightly affect the scattering magnitude but do not affect the directional pattern very much, which is determined mostly by the trunk and branches. The scattering contribution of the needles is very small and the needles can be either neglected or taken into account by adding the effective needle volume to the branches. For more accurate simulations, the needles can be accounted for without interaction terms. This produces results that are almost as accurate as those obtained from more advanced models.

6. Conclusions and future work

This work contributes to the rapidly developing field of Synthetic Aperture Radar (SAR) remote sensing and, especially, to coherent techniques relevant to forest remote sensing: polarimetry, interferometry, polarimetric interferometry and coherent scattering modeling. As mentioned in the introduction, microwave SAR can reveal information regarding forest regions which is not accessible by other remote sensing instruments. This is enabled by SAR wavelengths which are comparable in size to tree structures and by the coherent nature of the signal. Modern spaceborne SAR instruments, such as Terra-SAR-X and TanDEM-X, already provide high resolution images on a regular basis but the data are not yet used operationally in forest applications. The aim of this work is to bring recent advances of SAR technology to the use of boreal forest remote sensing. The main applications of the results presented in this work are relevant mostly for forest and biomass mapping; however several theoretical results can also be applied in other fields of SAR remote sensing. The presented algorithms can aid in global biomass map production and support national forest inventories. However, before operational use, further validation with larger data sets is necessary.

The work is presented in four main sections. Chapter 2 gives a short introduction to the radar remote sensing, Chapter 3 studies tools for polarimetric SAR image analysis, Chapter 4 develops a polarimetric interferometric SAR approach for forest height retrieval and Chapter 5 studies radar scattering from realistic tree geometries using theoretical models.

The improved approach to incoherent polarimetric target decomposition presented in Chapter 3 helps to reveal the information content in polarimetric SAR images and supports an improved understanding about connections between various polarimetric parameters and their physical significance. It is shown that traditional entropy and alpha parameters, of-

ten also used in studies concerning forest remote sensing, are very closely related to much simpler parameters and the eigenvalue calculation of coherency matrix is not required to extract this information. The proposed new parameters, *scattering diversity* and *surface scattering fraction*, perform equally well to traditional parameters in polarimetric SAR image analysis; however, they have as additional benefits less associated computation and a simpler physical interpretation. The new parameters also allow development of new improved visualization schemes which can be used for polarimetric SAR image interpretation, for example to detect deforestation in large scale polarimetric SAR images. This result shows that the eigenvector information provided by the coherency matrix eigendecomposition is not efficiently used in currently used decomposition parameters and should be further investigated in order to engage polarimetric information in the eigenvectors to their full extent.

Chapter 4 concentrates on the analysis of FINSAR airborne SAR campaign data. It demonstrates that tree height estimation based on polarimetric interferometry using L-band, a technique which was developed for tropical and temperate forest, also works well in the boreal zone. Additional analysis shows that X-band SAR interferometry can also be used for forest height retrieval. A careful comparison with LIDAR measured tree height reveals that X-band backscattering is arriving from the top third of the forest and the phase height correlates well with the canopy height. It is demonstrated that with the Random Volume over Ground model, the penetration depth can be calculated accurately and thus, when the ground model is available from other sources, forest height can be retrieved from X-band interferometric SAR images with a high accuracy. The same technique can be applied to L-band SAR measurements in order to reduce the need for fully polarimetric measurement or to improve RVoG inversion performance. The forest height estimation scheme proposed in this work potentially enables tree height measurement with TanDEM-X, the only available existing spaceborne interferometric X-band SAR system. Forest height is related to forest biomass through allometry equations and therefore tree height measurement from space would enable to produce more accurate global forest biomass maps. The method can give significant improvements to estimates, for example, in Finland, where a highly accurate ground model is available for the entire country free of charge. The work for validating the method with satellite data is already in progress.

The last part of the thesis focuses on understanding the microwave scat-

tering process inside the forest and trees in high detail. Chapter 5 demonstrates calculations of scattering from a realistic pine tree with accurate electromagnetic models. Modeling accuracy and validity range are assured by performing a cross comparison of the Infinite Cylinder Approximation (ICA) model with Volume Integral Equation (VIE) calculations. It is shown that a simpler infinite cylinder model, which does not account for interactions between cylinders, is sufficiently accurate at L-band in order to calculate scattering from a tree geometry which includes the trunk and branches. Accurate modeling of needles and interaction between needles does not significantly improve the result at L-band and lower frequencies. However, the same calculations at C-band reveal differences between the models, indicating that at C-band the needles and interaction between branches contributes to the scattering pattern, although the simpler model still performs well in general scattering pattern calculation. In the future the ICA scattering model should be developed further to include first order reflections between the cylinders and a more realistic ground model which accounts for ground roughness. In order to establish a relation between highly detailed models and a SAR measurement, a novel statistical approach is proposed. The presented theoretical results are not directly applicable as an operational forest monitoring algorithm; rather, the results deepen the understanding of scattering in forest and should yield better models in the future. The results can also help to determine the required level of modeling complexity so that accurate scattering simulations for trees is retained while substantially faster modeling can take place.

Bibliography

[1] J. Askne and M. Santoro. Multitemporal repeat pass SAR interferometry of boreal forests. *IEEE Trans. Geosci. Remote Sensing*, 43(6):1219–1228, 2005.

[2] M. Brandfass, C. Hofmann, J. C. Mura, and K. P. Papathanassiou. Polarimetric SAR interferometry as applied to fully polarimetric rain forest data. In *Proc. IEEE Int. Geoscience and Remote Sensing Symp. IGARSS '01*, volume 6, pages 2575–2577, Sydeny, Australia, 9–13 July 2001.

[3] W. C. Chew, E. Jin, J.-M. Michielssen, and J. Song, editors. *Fast and Efficient Algorithms in Computational Electromagnetics*. Artech House, Norwood, MA, 2001.

[4] Tsenchieh Chiu and K. Sarabandi. Electromagnetic scattering from short branching vegetation. *IEEE Trans. Geosci. Remote Sensing*, 38(2):911–925, 2000.

[5] S. R. Cloude. Uniqueness of target decomposition theorems in radar polarimetry. In W.-M. et al. Boerner, editor, *Proceedings of the NATO Advances Research Workshop on Direct And Inverse Methods in Radar Polarimetry*, volume 350 of *NATO ASI Series C*, pages 267–296, Bad Windsheim, Germany, September 18–24 1988. Kluwer Academic Publishers, Dordrecht 1992.

[6] S. R. Cloude. Polarization coherence tomography. *Radio Science*, 41:1–27, 2006.

[7] S. R. Cloude and K. P. Papathanassiou. Three-stage inversion process for polarimetric SAR interferometry. *IEE Proceedings - Radar, Sonar and Navigation*, 150(3):125–134, 2003.

[8] S. R. Cloude and E. Pottier. A review of target decomposition theorems in radar polarimetry. *IEEE Trans. Geosci. Remote Sensing*, 34:498–517, 1996.

[9] S. R. Cloude and E. Pottier. An entropy based classification scheme for land applications of polarimetric SAR. *IEEE Trans. Geosci. Remote Sensing*, 35(1):68–78, 1997.

[10] E. Colin-Koeniguer, N. N. Trouvé, and J. Praks. A review about alternatives to classical polarimetric SAR parameters. In *Proc. EUSAR, 8th European Conference on Synthetic Aperture Radar*, Aachen, Germany, 7–10 June 2010.

[11] E. Collett. *Field Guide to Polarization*, volume FG05 of *SPIE Field Guides*. SPIE, 2005.

[12] M. C. Dobson, F. T. Ulaby, T. LeToan, A. Beaudoin, E. S. Kasischke, and N. Christensen. Dependence of radar backscatter on coniferous forest biomass. *IEEE Trans. Geosci. Remote Sensing*, 30(2):412–415, 1992.

[13] Cao Fang, Hong Wen, and Wu Yirong. An improved Cloude-Pottier decomposition using H/α/SPAN and complex Wishart classifier for polarimetric SAR classification. In *International Conference on Radar, CIE '06*, Shanghai, China, 16–19 October 2006.

[14] A. Freeman and S. Durden. A three-component scattering model to describe polarimetric SAR data. *SPIE Radar Polarimetry*, 1748, 1992.

[15] A. Freeman and S. Durden. A three-component scattering model for polarimetric sar data. *IEEE Trans. Geosci. Remote Sensing*, 36(3):963–973, May 1998.

[16] F. Garestier, P. C. Dubois-Fernandez, and I. Champion. Forest height inversion using high-resolution P-band Pol-InSAR data. *IEEE Trans. Geosci. Remote Sensing*, 46(11):3544–3559, 2008.

[17] F. Garestier, P. C. Dubois-Fernandez, and K. P. Papathanassiou. Pine forest height inversion using single-pass X-band PolInSAR data. *IEEE Trans. Geosci. Remote Sensing*, 46(1):59–68, 2008.

[18] F. Garestier and T. Le Toan. Estimation of the backscatter vertical profile of a pine forest using single baseline P-band (Pol-)InSAR data. *IEEE Trans. Geosci. Remote Sensing*, 48(9):3340–3348, 2010.

[19] I. Hajnsek, F. Kugler, Seung-Kuk Lee, and K. P. Papathanassiou. Tropical-forest-parameter estimation by means of Pol-InSAR: The INDREX-II campaign. *IEEE Trans. Geosci. Remote Sensing*, 47(2):481–493, 2009.

[20] I. Hajnsek, K. P. Papathanassiou, and S. R. Cloude. Removal of additive noise in polarimetric eigenvalue processing. In *Proc. IEEE Int. Geoscience and Remote Sensing Symp. IGARSS '01*, volume 6, pages 2778–2780, Sydeny, Australia, 9–13 July 2001.

[21] M. Hallikainen, J. Hyyppä, J. Haapanen, T. Tares, P. Ahola, J. Pulliainen, and M. Toikka. A helicopter-borne eight-channel ranging scatterometer for remote sensing. I. System description. *IEEE Trans. Geosci. Remote Sensing*, 31(1):161–169, 1993.

[22] M. T. Hallikainen, F. T. Ulaby, M. C. Dobson, M. A. El-Rayes, and Lil-Kun Wu. Microwave dielectric behavior of wet soil-part 1: Empirical models and experimental observations. *IEEE Trans. Geosci. Remote Sensing*, (1):25–34, 1985.

[23] J. Hyyppä and M. Inkinen. Detecting and estimating attributes for single trees using laser scanner. *The Photogrammetric Journal of Finland*, 16(2):27–42, 1999.

[24] P. Imbo, J. C. Souyris, A. Lopes, and P. Marthon. Synoptic representation of the polarimetric information. In *Proceedings CEOS SAR Workshop*, volume 450 of *ESA-SP*, page 341, Toulouse, France, 26–29 October 1999.

[25] E. Kreyszig. *Advanced Engineering Mathematics*. John Wiley & Sons, INC., New York, 7 edition, 1993.

[26] R. G. Kuehni. *Color Space and Its Divisions: Color Order from Antiquity to the Present*. Wiley-Blackwell, 2003.

[27] F. Kugler, F. Koudogbo, K. Gutjahr, and K. Papathanassiou. Frequency effects in pol-insar forest height estimation. In *Proc. EUSAR, 6th European Conference on Synthetic Aperture Radar*, Dresden, Germany, 16–18 May 2006.

[28] R. H. Lang. Scattering from a layer of discrete random mediumover a random interface: Application to microwave backscatteringfrom forests. *Waves in Random Media*, (14):359–391, 2004.

[29] T. Le Toan, S. Quegan, M. W. J. Davidson, H. Balzter, P. Paillou, K. Papathanassiou, S. Plummer, F. Rocca, S. Saatchi, H. Shugart, and L. Ulander. The biomass mission: Mapping global forest biomass to better understand the terrestrial carbon cycle. *Remote Sensing of Environment*, 11(115):2850–2860, 2011.

[30] J.-S. Lee and E. Pottier. *Polarimetric Radar Imaging: From Basics to Applications*. CRC Press, Taylor & Francis Group, 2009.

[31] J.S. Lee, M. R. Grunes, T. L. Ainsworth, L. Du, D.L. Schuler, and S. R. Cloude. Unsupervised classification using polarimetric decomposition and complex Wishart classifier. In *Proc. IEEE Int. Geoscience and Remote Sensing Symp. IGARSS'98*, volume 4, pages 2178–2180, Seattle, USA, 6–10 July 1998.

[32] Yi-Cheng Lin and K. Sarabandi. A Monte Carlo coherent scattering model for forest canopies using fractal-generated trees. *IEEE Trans. Geosci. Remote Sensing*, 37(1):440–451, 1999.

[33] Yi-Cheng Lin and K. Sarabandi. Retrieval of forest parameters using a fractal-based coherent scattering model and a genetic algorithm. *IEEE Trans. Geosci. Remote Sensing*, 37(3):1415–1424, 1999.

[34] Dawei Liu, Guoqing Sun, Zhifeng Guo, K. J. Ranson, and Yang Du. Three-dimensional coherent radar backscatter model and simulations of scattering phase center of forest canopies. *IEEE Trans. Geosci. Remote Sensing*, 48(1):349–357, 2010.

[35] M. Luckiesh. *Color and its applications*. D. Van Nostrand company, 1921.

[36] E. Luneburg, S. R. Cloude, and W.-M. Boerner. On the proper polarimetric scattering matrix formulation of the forward propagation versus backscattering radar systems description. In *Proc. IEEE Int. Geoscience and Remote Sensing Symp. IGARSS'97*, volume 4, pages 1591–1593, Singapore, 3–8 August 1997.

[37] T. Mette, F. Kugler, and K. Papathanassiou. Forest and the random volume over ground – nature and effect of 3 possible error types. In *Proc. EUSAR, 8th European Conference on Synthetic Aperture Radar*, Dresden, Germany, 16–18 May 2006.

[38] T. Mette, K. Papathanassiou, and I. Hajnsek. Biomass estimation from polarimetric SAR interferometry over heterogeneous forest terrain. In *Proc. IEEE Int. Geoscience and Remote Sensing Symp. IGARSS'04*, volume 1, pages 511–514, Anchorage, USA, 20–24 September 2004.

[39] C. Oliver and S. Quegan. *Understanding Synthetic Aperture Radar Image*. Artech House, Inc., 1998.

[40] K. P. Papathanassiou and S. R. Cloude. Single-baseline polarimetric SAR interferometry. *IEEE Trans. Geosci. Remote Sensing*, 39(11):2352–2363, 2001.

[41] P. Penman, M. Gytarsky, T. Hiraish, T. Krug, and D. Kruger, editors. *Good Practice Guidance for Land Use, Land Use Change and Forestry*. The Intergovernmental Panel on Climate Change, IPCC, 2003.

[42] J. Perttunen. *The LIGNUM functional-structural tree model*. PhD thesis, Helsinki University of Technology, 2009.

[43] J. Perttunen, R. Sievänen, and E. Nikinmaa. LIGNUM: A model combining the structure and the functioning of trees. *Ecological Modelling*, 108:189–198, 1998.

[44] J. Praks, P. Ahtonen, M. Engdahl, and Hallikainen M. Modelled polarimetric backscattering response from single pine trees and pine canopies. In *Proc. POLinSAR'03, International Workshop on Applications of Polarimetry and Polarimetric Interferometry*, ESA-ESRIN, Frascati, Italy, 14–16 January 2003.

[45] J. Praks, A. N. Arslan, H. Alasalmi, J. Koskinen, and M. Hallikainen. SAR target decomposition for stochastic natural targets for L- and C-band. In *Proc. IEEE Int. Geoscience and Remote Sensing Symp. IGARSS'99*, volume 3, pages 1558–1560, Hamburg, Germany, 28 June–2 July 1999.

[46] J. Praks and M. Hallikainen. A novel approach in polarimetric covariance matrix eigendecomposition. In *Proc. IEEE Int. Geoscience and Remote Sensing Symp. IGARSS'00*, volume 3, pages 1119–1121, Honolulu, USA, 24–28 July 2000.

[47] J. Praks and M. Hallikainen. Entropy-alpha classification alternative for polarimetric SAR image. In *Proc. POLinSAR'03, International Workshop on Applications of Polarimetry and Polarimetric Interferometry*, ESA-ESRIN, Frascati, Italy, 14–16 January 2003.

[48] J. Praks and M. Hallikainen. Combining high resolution and low resolution information in synoptic representation of fully polarimetric SAR images. In *Proc. POLinSAR'05, 2nd International Workshop on Applications of Polarimetry and Polarimetric Interferometry*, ESA-ESRIN, Frascati, Italy, 17–21 January 2005.

[49] J. Praks, M. Hallikainen, and E. C. Koeniguer. Polarimetric SAR image visualization and interpretation with covariance matrix invariants. In *Proc. IEEE Int. Geoscience and Remote Sensing Symp. IGARSS'10*, pages 2035–2038, Honolulu, USA, 25–30 July 2010.

[50] J. Praks, M. Hallikainen, F. Kugler, K. Papathanassiou, and I. Hajnsek. L-band polarimetric interferometry in boreal forest parameter estimation,

a case study. In *Proc. IEEE Int. Geoscience and Remote Sensing Symp. IGARSS'06*, pages 2216–2219, Denver, Colorado, USA, 31 July–4 August 2006.

[51] J. Praks, M. Hallikainen, F. Kugler, and K. P. Papathanassiou. Coherence tomography for boreal forest: Comparison with HUTSCAT scatterometer measurements. In *Proc. EUSAR, 7th European Conference on Synthetic Aperture Radar*, pages 1–4, Friedrichshafen, Germany, 2–5 June 2008.

[52] J. Praks, M. Hallikainen, F. Kugler, and K.P. Papathanassiou. X-band extinction in boreal forest: Estimation by using E-SAR POLInSAR and hutscat. In *Proc. IEEE Int. Geoscience and Remote Sensing Symp. IGARSS'07*, pages 1128–1131, Barcelona, Spain, 23–27 July 2007.

[53] J. Praks, M. Hallikainen, J. Seppänen, and J. Hyyppä. Boreal forest height estimation with SAR interferometry and laser measurements. In *Proc. IEEE Int. Geoscience and Remote Sensing Symp. IGARSS'09*, volume 5, pages 308–311, Cape Town, South Africa, 12–17 July 2009.

[54] J. Praks, F. Kugler, J. Hyyppä, K. Papathanassiou, and M. Hallikainen. SAR coherence tomography for boreal forest with aid of laser measurements. In *Proc. IEEE Int. Geoscience and Remote Sensing Symp. IGARSS'08*, volume 2, pages 469–472, Boston, USA, 7–11 July 2008.

[55] J. Praks, J. Pulliainen, P. Ahtonen, and M. Hallikainen. Examination of forest polarimetric backscattering with coherent cylinder model. In *Proc. IEEE Int. Geoscience and Remote Sensing Symp. IGARSS'03*, volume 2, pages 923–925, Toulouse, France, 21–25 July 2003.

[56] J. Praks, J. Sarvas, M. Hallikainen, and J. Pulliainen. Utilization of coherent forest scattering model in polarimetric sar measurement interpretation. In *Proc. XXVIIIth URSI General Assembly*, New Delhi, India, 23–29 October 2005.

[57] P. Prusinkiewicz and A. Lindenmayer. *The algorithmic beauty of plants*. Springer-Verlag, New York, USA, 1990.

[58] S. Quegan and I. Rhodes. Statistical models for polarimetric data: consequences, testing and validity. *Int. J. Remote Sensing*, 16(7):1183–1210, 1995.

[59] K. Sarabandi and Y.-C. Lin. Simulation of interferometric SAR response for characterizing the scattering phase center statistics of forest canopies. *IEEE Trans. Geosci. Remote Sensing*, 38(1):115–125, 2000.

[60] J. Sarvas, J. Praks, L. M. Zurk, P. Koistinen, M. Hallikainen, J. Pulliainen, and L. Holmström. A polarimetric forest scattering model based on truncated infinite cylinder approximation. Unpublished.

[61] S. S. Seker and A. Schneider. Electromagnetic scattering from a dielectric cylinder of finite length. *IEEE Trans. Antennas Propagation*, 36:303–307, 1988.

[62] R. Sessa and H. Dolman, editors. *Terrestrial Essential Climate Variables for Climate Change Assessment, Mitigation and Adaptation*. GTOS-52, FAO, Rome, 2008.

[63] C. E. Shannon. A mathematical theory of communication. *Bell System Technical Journal*, 27:379–423, 623–656, 1948.

[64] Wu. Shih-Tseng. Potential application of multipolarization SAR for pine-plantation biomass estimation. *IEEE Trans. Geosci. Remote Sensing*, 25(3):403–409, 1987.

[65] E. M. W. Smeets and A. P. C. Faaij. Bioenergy potentials from forestry in 2050. *Climatic Change*, 81(3–4):353–390, 2007.

[66] Guoqing Sun and K. J. Ranson. A three-dimensional radar backscatter model of forest canopies. *IEEE Trans. Geosci. Remote Sensing*, 33(2):372–382, 1995.

[67] L. Thirion, I. Chênerie, and Galy C. Application of a coherent model in simulating the backscattering coefficient of a mangrove forest. *Waves in Random Media*, 14:299–316, 2004.

[68] L. Thirion, E. Colin, and C. Dahon. Capabilities of a forest coherent scattering model applied to radiometry, interferometry, and polarimetry at P- and L-band. *IEEE Trans. Geosci. Remote Sensing*, 44(4):849–862, 2006.

[69] R. N. Treuhaft, B. D. Chapman, J. R. Dos Santos, F. G. Goncalves, F. G.alves, L. V. Dutra, P. M. L. A. Graca, and J. B. Drake. Vegetation profiles in tropical forests from multibaseline interferometric synthetic aperture radar, field, and lidar measurements. *J. Geophys. Res. D Atmos.*, 114(23):1–16, 2009.

[70] R. N. Treuhaft, B. E. Law, G. P. Asner, and S. Hensley. Vegetation profile estimates from multialtitude, multifrequency radar interferometric and polarimetric data. In *Proc. IEEE Int. Geoscience and Remote Sensing Symp. IGARSS'00*, volume 1, pages 126–128, Honolulu, USA, 24–28 July 2000.

[71] R. N. Treuhaft, S. N. Madsen, M. Moghaddam, and J. J. Van Zyl. Vegetation characteristics and underlying topography from interferometric radar. *Radio Science*, 31(6):1449–1485, 1996.

[72] M. L. Williams. The theory for a forward SAR model: Implementation, applications and challenges. In *Proc. EUSAR, 6th European Conference on Synthetic Aperture Radar*, Dresden, Germany, 16–18 May 2006.

[73] I. H. Woodhouse, S. Cloude, K. Papathanassiou, J. Hope, J. Suarez, P. Osborne, and G. Wright. Polarimetric interferometry in the Glen Affric project: results & conclusions. In *Proc. IEEE Int. Geoscience and Remote Sensing Symp. IGARSS'02*, volume 2, pages 820–822, Toronto, Canada, 24–28 June 2002.

[74] D. Zianis, P. Muukkonen, R. Mäkipää, and M. Manuccini. Biomass and stem volume equations for tree species in Europe. *Silva Fennica Monographs*, 4:1–63, 2005.

[75] L. M. Zurk, P. Koistinen, J. Sarvas, and L. Holmström. Electromagnetic scattering model for forest remote sensing. Research Reports A38, Rolf Nevanlinna Institute, 2002.

Errata

Publication I

In page 2263, equation (11) should be $p_i = \frac{\lambda_i}{\sum_{n=1}^{3} \lambda_n}$

Publication I

In page 2271, terms *hue* and *saturation* have unfortunately switched places in one sentence. The second sentence of the third section should be: The *saturation* of the image is controlled by entropy (averaged over a 20×20 window); the *hue* is determined by the $\bar{\alpha}$ angle (averaged over a 4×4 window) and the intensity is log(span) (averaged over a 4×4 window).

Modern times need modern tools to monitor and manage our living environment, our planet. Microwave radar satellites is a class of rapidly developing remote sensing instruments whose full capability has not yet been unleashed. In this work the author develops and demonstrates coherent SAR image analysis techniques for boreal forest applications to help in global biomass mapping.

Aalto-DD 153/2012

ISBN 978-952-60-4872-7
ISBN 978-952-60-4873-4 (pdf)
ISSN-L 1799-4934
ISSN 1799-4934
ISSN 1799-4942 (pdf)

Aalto University
School of Electrical Engineering
Department of Radio Science and Engineering
www.aalto.fi